

Physical Properties of PVDF-GO/Black-TiO₂ Nanofibers and its Photocatalytic Degradation of Methylene Blue and Malachite Green Dyes

M K Abdelmaksoud

Cairo University

Alaa Mohamed (✉ alakha@kth.se)

Karlsruhe Institute of Technology: Karlsruher Institut für Technologie <https://orcid.org/0000-0002-1439-8617>

Abderrahman Sayed

Cairo University

S A Khairy

Cairo University

Research

Keywords: Black-TiO₂, Graphene Oxide, Photocatalytic activity, Water treatment, Optical energy bands, Redox reaction mechanism

Posted Date: December 1st, 2020

DOI: <https://doi.org/10.21203/rs.3.rs-113863/v1>

License:  This work is licensed under a Creative Commons Attribution 4.0 International License.

[Read Full License](#)

Physical properties of PVDF-GO/Black-TiO₂ nanofibers and its Photocatalytic degradation of Methylene Blue and Malachite Green dyes

M K Abdelmaksoud^{a,b}, Alaa Mohamed^{c,d,*}, Abderrahman Sayed^{a,b}, S A Khairy^a

^a Physics Department, Faculty of Science, Cairo University, Giza, Egypt.

^b Faculty of Nanotechnology for postgraduate studies, Cairo University, El-Sheikh Zayed 12588, Egypt.

^c Department of Mechatronics, Canadian International College, Fifth Settlement, New Cairo, Egypt

^d Institute of Functional Interfaces (IFG), Karlsruhe Institute of Technology (KIT), Hermann-von-Helmholtz-Platz 1, 76344 Eggenstein-Leopoldshafen, Germany

Corresponding author: Dr. Alaa Mohamed*

Email: alakha@kth.se

Abstract

Background: Black TiO₂ and Graphene Oxide (GO) have attracted intensive attention as an effective catalyst on visible light driven for photodegrading of dyes. In this study, nano-black TiO₂ was prepared by a simple hydrogenation of the anatase titanium oxide and the graphene oxide was prepared by applying the modified Hummers method. The prepared powders and nanofiber membranes are carefully examined to ensure their single phase and compound structure formation as well as to measure the equivalent crystallite size and particle distributions.

Results: The optimum degradation efficiency of malachite green and methylene blue dyes occurred at pH values of 8 and 10, respectively. Afterwards, at the optimum pH value of 8, for malachite green, the degradation efficiency is peaked at 20 mg of the nano-black TiO₂ concentration. Then, a comparison of the degradation efficiency of the two mentioned dyes are performed as the fore-mentioned nanofibers are loaded with 20 mg nano-black TiO₂ at the corresponding optimum pH vales.

Conclusions: The diffuse reflectance spectroscopy has been investigated to find out the optical energy gaps of the treated and nano-black samples. Finally, a schematic of the redox reaction mechanism has been proposed.

Keywords: Black-TiO₂; Graphene Oxide; Photocatalytic activity; Water treatment; Optical energy bands; Redox reaction mechanism.

1. Background:

Industrial wastewaters, especially from textile, pharmaceutical, cosmetic, pulp and paper as well as food processing industries, usually contain large amounts of dye contaminants [1, 2]. As many dyes are toxic and even carcinogenic, the discharge of dye containing wastewaters to the environment certainly poses a serious threat to the environment [3]. Titanium dioxide (TiO₂) nanoparticle has been extensively investigated for numerous applications, for example, a white pigment [4], UV absorber in sunscreens [5], photocatalyst for hydrogen generation [6], environmental pollution removal [7, 8] as well as photo-electrochemical sensors [9, 10]. Moreover, it is considered as one of the well-known catalyst as a consequence of its availability, low-cost, non-toxicity and relatively high chemical stability [11, 12]. It exists in

three crystalline phases, namely, tetragonal anatase, tetragonal rutile and orthorhombic brookite [13]. As a result of their higher photoactivity, both of the two phases, rutile and anatase have been widely used [14]. Nevertheless, they absorb only the UV-light, since their band gap energies are somewhat wide, 3.2 and 3.0 eV for anatase and rutile phases respectively [15]. Besides, TiO₂ show a low quantum efficiency since the photo-generated electron-hole pairs are rapidly recombined [16]. Therefore, to improve the photocatalytic activity of TiO₂, it is essential to improve its optical absorption range and charge separation. As a solution to the mentioned complications, hydrogenation was applied and black TiO₂ was first prepared in 2011 showing an extended absorption range down to infrared region [17]. Moreover, the structural, chemical, electronic and optical properties of TiO₂ nanoparticles have been radically changed through hydrogenation. Furthermore, graphene oxide (GO) has a low band gap and high conductivity properties which improve the catalytic properties [18, 19].

Large scale processing and widespread use of synthetic dyes cause significant contamination to the atmosphere [12]. Dyes are used in both commercial and analytical fields and are biologically and chemically difficult to decompose [7]. It is applied as a histological dye, an antifungal drug, a carcinogenic agent, a teratogenic agent, an environmental contaminant, and an antibacterial agent, causing extreme effects in water bodies because it decreases light penetration and thus leading to a demise of aquatic life [20, 21]. These dyes escape from traditional water treatment processes and stay in the environment. Nanofibers with controllable structural characteristics such as diameter, pore size and pore ratio were manufactured by adjusting the processing parameters in the electrospinning technique [22, 23]. Poly(vinylidene fluoride) (PVDF) is a polymer with desirable behaviors including high mechanical, chemical, and thermal stability properties. Different processing methods of PVDF leads to five crystalline polymorphs phases [24]. Two of these polymers are non-polar, whereas, the other three are polar and demonstrate ferroelectric and piezoelectric properties[25]. α , β and γ phases are the most frequently explored as a result of their properties and widespread applications [26]. This work investigates the synthesis of black-TiO₂, GO, electrospun of PVDF-GO nanofiber, and PVDF-GO/black-TiO₂ composite nanofiber membrane for the photocatalytic degradation of malachite green (MG) and methylene blue (MB) under visible light. The effect of various parameters such as pH, initial dyes concentration, contact time, and catalyst dose was evaluated. Nanofibers are recyclable which makes this technique in wastewater treatment cheap and green.

2. Experimental

2.1 Materials

Titanium dioxide (TiO₂, Anatase powder 98%), Sodium hydroxide pellets (NaOH, 98%) and Sodium borohydride (NaBH₄, 95%) from ADVENT CHEMBIO PVT LTD, Sodium chloride (NaCl, 98.5%) from Egyptian salt and minerals Co., Graphite powder (particle size 150 mesh 90% min) from Nice chemicals LTD., Sulfuric acid (H₂SO₄, 98%) from S D Fine Chem LTD., Potassium permanganate (KMnO₄, 98%) from El Goumhouria, Egypt, Hydrogen peroxide

(H₂O₂, 30%) from PioChem for laboratory chemicals, Hydrochloric acid (HCl, 37% from Honeywell Specialty Chemicals Seelze, Germany, Acetone (2-propanon, 99.5%) from Diachem, N,N-dimethyl formamide (DMF, 99%) from Alfa Aesar, Poly(vinylidene fluoride) (PVDF) pellets (M_w = 275000) from Sigma-Aldrich, Glutaraldehyde (GA, 50%) from Fine Chemicals, Ethyl alcohol (Ethanol, 99%) from PioChem for laboratory chemicals, malachite green (MG) from Sigma Aldrich and methylene blue (MB) from science lab.

2.2 Preparation of treated TiO₂ nanoparticles:

2.5 g of anatase TiO₂ bulk powder was dissolved into 150 ml NaOH solution (10 M) at room temperature, applying vigorous stirring for 2 h. Then, the solution was placed in ambient temperature for 2 h in an ultrasonic bath (Sonica 4200, 40 kHz and 800 W). The precipitates were centrifuged then washed with deionized water until the solution is neutralized. Afterward, the precipitates were dried at 120 °C [27].

2.3 Preparation of nano-black TiO₂ (NB):

TiO₂ and NaBH₄ with a respective molar ratio of 1:2 were mixed. Specifically, 0.7987 g of anatase TiO₂ and 0.7566 g of NaBH₄ were mixed thoroughly, then the mixture was grinded for 15 min to homogenize it. Afterwards, a small stainless autoclave was used to heat the mixture up to 325 °C for 16 h. As a substitute of the vacuum system with Ar atmosphere, the mixture was perfectly fit in between a double layer of NaCl powder to make sure that the mixture is chemically isolated. Finally, the black TiO₂ was dried at 120 °C, after being washed repeatedly with distilled water to neutralize the solution.

2.4 Preparation of graphene oxide (GO):

An excessive oxidation technique of graphite by adding KMnO₄ and H₂SO₄ has been utilized to synthesize GO which is known as the modified Hummers method. Explicitly, graphite powder (2 g) was stirred in 98% H₂SO₄ (45 mL) for 1 h. Then a 6 g of KMnO₄ was gradually added to the above solution while keeping the temperature at less than 20 °C through an ice bath. After the temperature has been stabilized, the solution was kept stirring at room temperature for another 1.5 h. The solution put back into the ice bath and diluted through the addition of 90 mL of distilled water, keeping a forceful stirring. Furthermore, 30% H₂O₂ solution (10 mL) and distilled water (150 mL) were added while maintaining the stirring. Repeated centrifugation was employed to wash the graphene oxide (GO), mainly with 5% HCl aqueous solution followed by distilled water until the solution pH became neutral. GO was then dried under 60 °C to prevent changing to reduced graphene oxide (RGO).

2.5 Preparation of PVDF-GO nanofiber:

The electrospinning method has been applied to synthesize PVDF-GO nanofiber membranes. The applicable solution with 20 wt% of PVDF pellets and 0.3 wt% of GO were mixed together into a DMF/acetone (v/v 3/2) solvent and the resulting solution was placed into a sonicator for

15 min. Then, the prepared solution was stirred at a temperature lower than 60 °C for 2h to obtain a homogeneous solution. The solution was then filled into a 5mL syringe with a 22 gauge needle. The syringe was positioned vertically for a minute and the air was completely removed by pushing the end of the syringe plunger. The flow rate was controlled by NE-300 (New Era Pump System Inc.) and the voltage supply equipment used was a 73030N (Genvolt General High Voltage Ind. Ltd.). The following conditions were employed: a flow rate of 1 mL/h, a voltage of 23.5 kV and a TCD (tip to collector distance) of 15 cm. As a last step, the membrane was left to dry at room temperature.

2.6 Preparation of PVDF-GO/NB-TiO₂ composite nanofibers:

An area of 3×3 cm² PVDF-GO composite nanofiber was submerged into the crosslinking medium with 2.5 wt. % Glutaraldehyde (GA) and was kept soaking at room temperature for 20 h. The NB NPs quantity (5, 10 and 20 mg) was then added to 7 ml of distilled water and the solution was placed into an ultrasonic bath for 15 min. After the membrane was dried, the ultrasonicated solution was added to the composite nanofiber into a 4 cm diameter petri dish, which was kept shaking in an orbital shaker SO1 (Stuart Scientific) for 17 h. The cross-linked composite nanofibers were dried, then washed out with deionized water and ethanol and left to dry at room temperature. Figure 1 represented the schematic of the composite nanofiber membrane preparation.

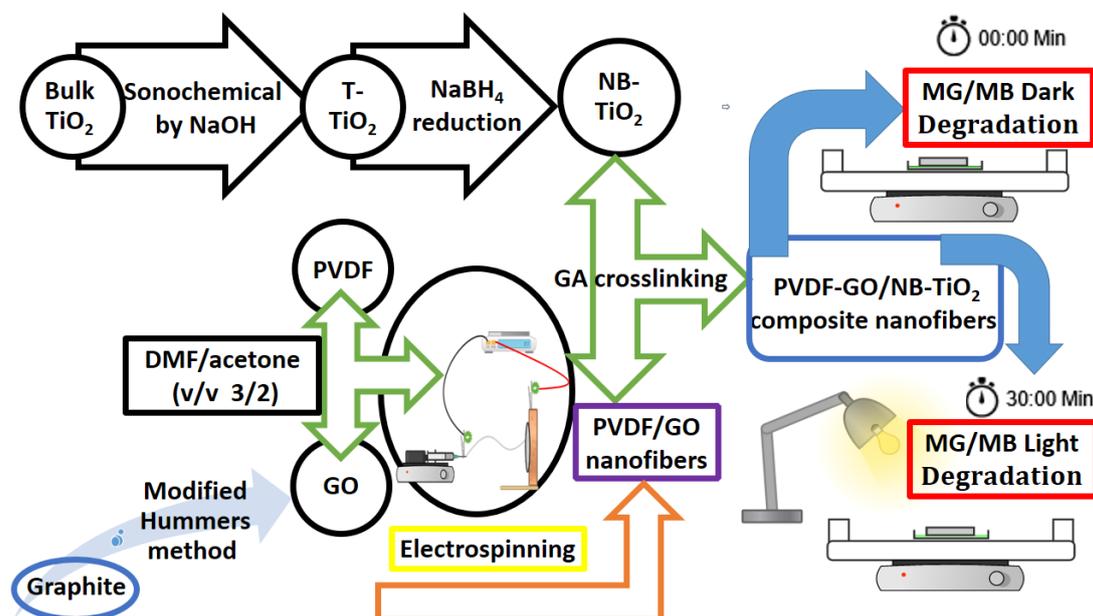


Fig. 1. A schematic of the preparation techniques and the experimental procedure followed in this study.

2.7 Photodegradation experiments:

The experiments were carried out by placing the NB cross-linked 3×3 cm² nanofiber into a 9-cm diameter petri dish containing dyes solution (50 mL) and continue shaking at 100 rpm on the orbital shaker. We started collecting the data, 30 min in the dark before switching the lamp

on, afterwards, the solution was illuminated by 500W Halogen lamp which is located 50 cm away from the sample. 2 mL of the dye solution was withdrawn from the dish after 30 min of dark shaking and then at a fixed interval of time and transferred to a glass tube and tested by UV-vis/NIR Spectrophotometer to calculate the visible light photocatalytic degradation of the dye. The degradation efficiency of dyes was calculated by the following equation:

$$\text{Degradation efficiency } (\eta) = \left(\frac{C_0 - C}{C_0} \right) \times 100\%$$

Where, C_0 and C represent the dye concentration before and after irradiation and are measured in mg/L. To study the effect of pH, the degradation efficiency was investigated for different pH values of 4, 6, 8 and 10. The solution pH value is controlled by the addition of NaOH (0.1 M) and HCl (0.1 M) solution.

2.8 Characterization

Particles morphology were measured by High-resolution transmission electron microscopy, HRTEM, JEM-2100, jeol. Scanning electron microscopy was carried out using FE SEM-Quanta FEG-250, Thermo Fisher Scientific. Whereas, the X-ray powder diffraction calculations were performed on D8 Discover, Bruker, where Cu $K\alpha$ radiation was used with wavelength of 1.540 Å. Fourier-transformed infrared spectroscopy spectra were recorded on Nicolet 6700 FT-IR with smart ITR, Thermo Scientific. The contact angle of nano composite were measured by One Attention Ver. 2.7 (r5433), Biolin Scientific. The UV-Visible/NIR Spectrophotometers for diffusion reflectance spectroscopy is obtained through the application of Jasco V570, JASCO. The dyes absorbance for MG ($\lambda_{\max} = 617$ nm) and MB ($\lambda_{\max} = 668$ nm) samples were recorded by Single beam visible spectrophotometer, Jenway 6300, Cole-Parmer, where deionized water has been used as a reference sample.

3. Results and discussion

3.1 Materials characterization

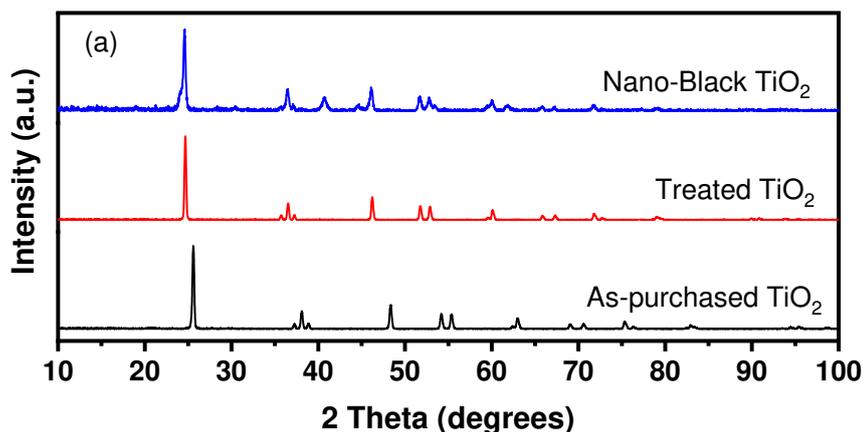
Applying Bragg's law of diffraction at a specific group of planes with a known inter-planar distance to find the samples lattice constants (a, b and c) from the XRD scans. Then, the unit cell volume (V) and the theoretical density D as given by $D = \frac{ZM}{N_A V}$, where Z is the number of molecules per unit cell, M is the molecular weight, N_A is Avogadro's number, are directly calculated. Moreover, the average crystallite size (D_x) of the investigated samples was calculated by applying Debye–Scherrer equation [28]: $D_x = \frac{k\lambda}{\beta \cos\theta}$ where λ is the Cu- $k\alpha$ wavelength, k is the shape factor, whose usual value is 0.89, β is the full width at half maximum (FWHM) in radians and θ is the diffraction angle. Table (1) shows that the structural parameters, specifically, the average crystallite size, the lattice constants and the unit cell volume of the treated (T) sample is slightly larger than those of the as-purchased anatase sample. While the nano-black TiO₂ (NB) displays the least average crystallite size, its lattice

constants and unit cell volume relatively expand. Therefore, the NB density shows the minimum value of all samples [29].

Table 1 Average crystal size (D_x), lattice constants, unite cell volume and theoretical density for as purchased anatase, treated and nano-black TiO_2 samples.

TiO ₂ Sample	Average grain size from (SEM) (nm)	Average crystallite size (D_x) (nm)	Lattice constants			Unit cell volume (v) (nm ³)	Theoretical density (D) (g/cm ³)
			a (nm)	b (nm)	c (nm)		
As-purchased anatase (AP)	---	32.3	0.37607	0.37607	0.94378	0.13348	3.97427
Treated (T)	110 ± 32	32.4	0.37689	0.37689	0.94572	0.13434	3.94887
Nano-Black (NB)	124 ± 33	25.3	0.37772	0.37772	0.94809	0.13527	3.92173

Fig. 2a shows the x-ray diffraction of the as-purchased, treated (T) and nano-black (NB) TiO_2 . The scans demonstrate the crystallinity and the single phase formation of the three oxides. XRD patterns show relatively strong diffraction peaks at around 25° and 48° which are indications of the anatase phase [30]. Fig. 2b shows the deviation of the peak position around 25.6°. The peak shift of the T and NB samples are toward smaller angles. This is consistent with the variations of the lattice parameters in table 1. Fig. 2c displays X-ray diffraction of GO, PVDF nanofiber, PVDF-GO nanofiber (0.3% GO), and PVDF-GO/NB- TiO_2 (0.3% GO with 20 mg NB- TiO_2). For GO a sharp peak at 10° was correlated to the (001) inter-layer structure of GO sheets [31]. The PVDF nanofiber has a strong two peak at 20.3° and 18.5° corresponds to (110/101) and (020) of monoclinic crystal, respectively [32]. For the composite nanofiber membrane the diffraction peaks at 25.3, 37.8, 47.9, 53.8, 55.0, 62.9, can be indexed to the anatase phase of TiO_2 [33].



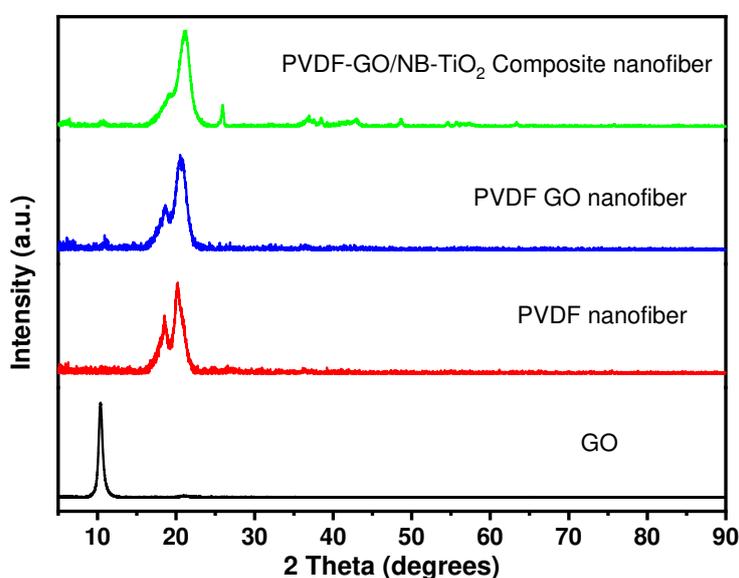
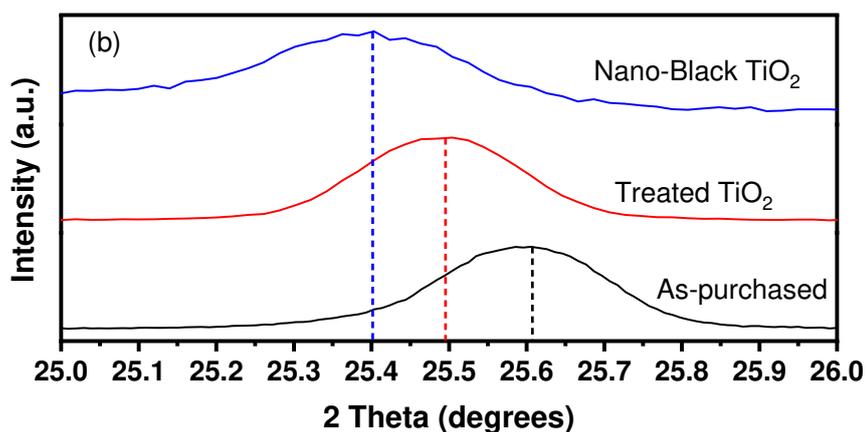


Fig. 2 a) X-ray diffraction of as-purchased, treated (T) and nano-black (NB) TiO_2 , b) Deviation of the peak position around 25.6° and c) XRD of GO, PVDF nanofiber, PVDF-GO nanofiber, and PVDF-GO/NB- TiO_2 .

For the AP and T-samples, Fig. 3a unveils that the transmittance is relatively low up to a wavenumber of about 730 cm^{-1} . In the range 800 to 4000 cm^{-1} , the transmittance is rather high for the as-purchased sample and even higher for the treated TiO_2 . Whereas, the NB sample shows a peak of the transmittance at about 900 cm^{-1} and much lower values for higher wavenumbers. This means that the absorbance of NB- TiO_2 over the designated wavelength range is substantially higher than that of the other two samples. These observations may be explained by the dependence of the band intensity on the change of the dipole moment as a result of atoms displacement and on its degree of anharmonicity [34, 35].

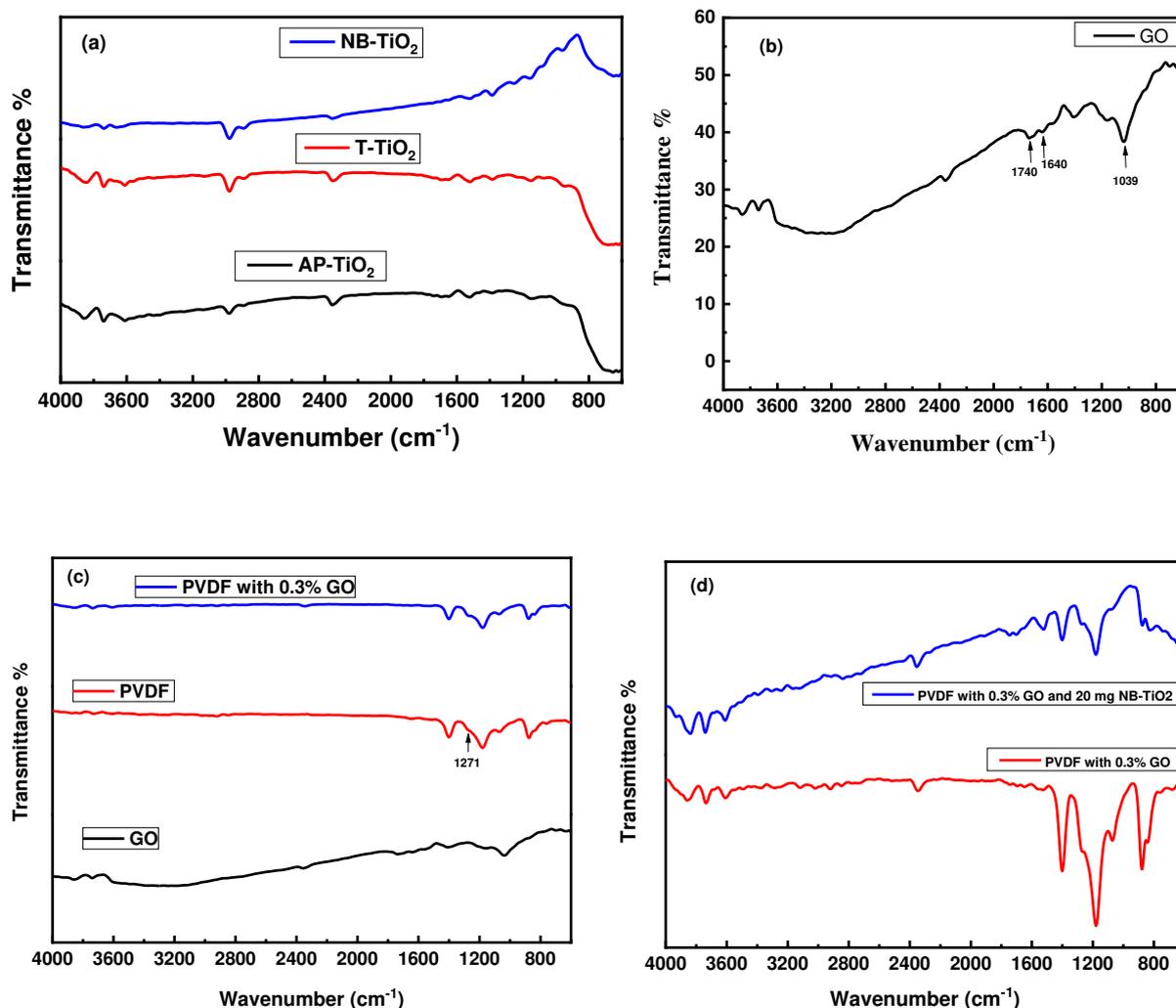


Fig. 3. FTIR of a) AP, T and NB-TiO₂, b) prepared GO, c) GO, PVDF nanofiber and PVDF nanofiber with 0.3% GO and d) PVDF nanofiber with 0.3% GO and PVDF nanofiber with 0.3% GO doped with 20 mg NB-TiO₂.

The functional groups of the investigated samples are inspected by FTIR. The fingerprint region of any FTIR spectrum lies in the range 400 to 1500 cm⁻¹ since it is the usual range used to identify the dissimilar compounds. In this study, the first fingerprint band, around 725 cm⁻¹, is associated with the bond Ti-O-Ti in the anatase phase [36]. Additionally, the other characteristic band at 915 cm⁻¹, is ascribed to the Ti-O vibrations [37]. Knowing that, even at normal conditions, the TiO₂ surface interacts promptly with water, which in turn has a substantial influence on surface processes, such as photo-catalysis [38]. Specifically, the band in the range 3800-3600 cm⁻¹ is attributed to stretching vibrations of OH groups, besides various OH groups on TiO₂ are marked by the bands 3720 to 3620 cm⁻¹ [39]. The band around 3600 cm⁻¹ is indicative of a “free” OH group, and it may be residing on the surface, or encapsulated within the crystal lattice [40]. The spectra also display two prominent bands around 3400 (O-H stretching) and 1645 cm⁻¹ (H-O-H) bending [41]. Moreover, the existence of moderate to intense bands in the ranges 1600–1300, 1200–1000 and 800–600 cm⁻¹ is an indication of a simple hydroxyl compound. The nano-black sample displays in addition to the bands that correspond to Ti-O-Ti bond and Ti-O vibrations, an extra band, rather small, at around 3670 cm⁻¹ due to hydrogenation [42]. Generally, the band 1700–1600 cm⁻¹ is due primarily to the C=O stretching vibration. And the two bands 3000 to 2800 cm⁻¹ and 1500 to 1300 cm⁻¹

correspond to C-H simple stretching and bending vibrations, respectively [40]. Furthermore, the band around 2350 cm^{-1} indicates chemisorbed CO_2 [43]. Normally, the presence of OH and CO functional groups are predicted since measurements are performed in-air. Fig. 4.b shows the specific, slightly shifted, peaks that characterize the prepared GO [44]. The PVDF used in this study is most likely to be β -phase as a result of the existence of 1271 cm^{-1} band, Fig. (4-c) and following the flow chart for the identification of α , β and γ phases [32]. Fig. 4.d display FTIR of PVDF nanofiber with 0.3 % GO with and without 20 mg of TiO_2 .

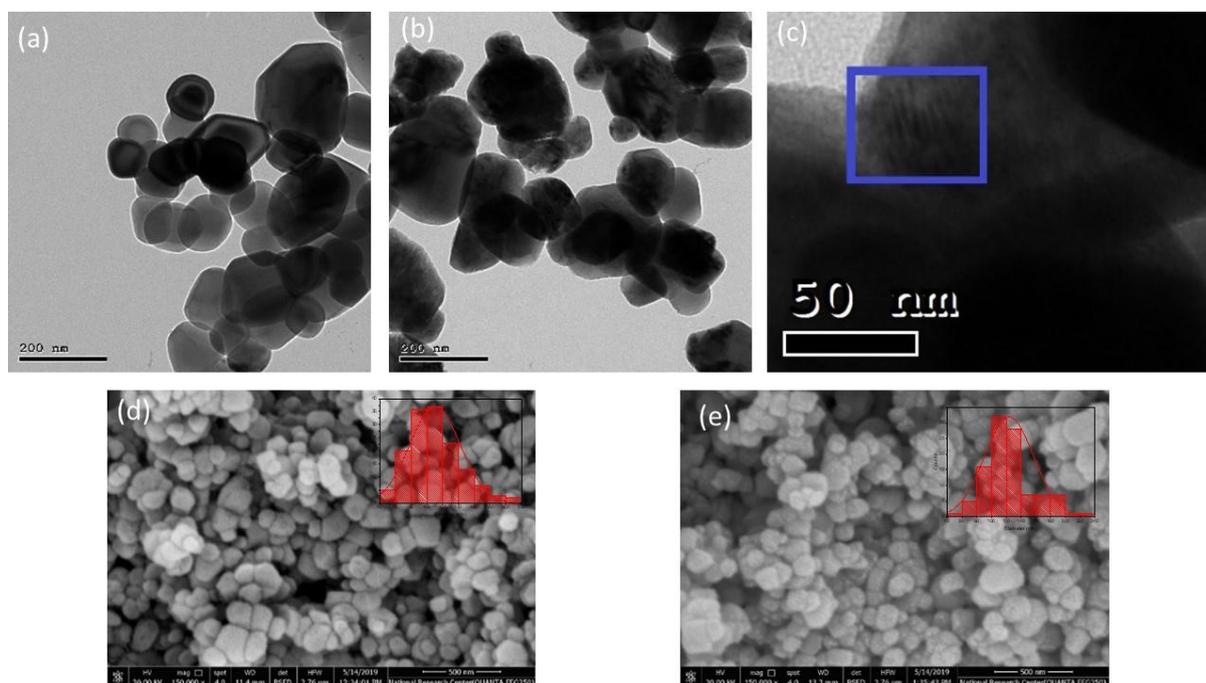


Fig. 4. HRTEM of a) T- TiO_2 , b) NB- TiO_2 and c) Moiré fringes in NB sample, FESEM of d) Treated and e) NB- TiO_2 nanoparticles, with the corresponding particles distribution as insets.

Generally, HRTEM and FESEM are valuable at inspecting the morphology and the crystallinity of the sample, as well as the particle size. Depending on the synthesis procedure, dissimilar types of morphology were designated including nanotubes [45], wires [46], spheres [47], spike [48]. A defective surface layer of hydrogenated TiO_2 , as well as a crystalline core and amorphous shell structure, have been confirmed by many researchers. The common observed defects on the black- TiO_2 surface are Ti^{3+} ions and oxygen vacancies [49]. For HRTEM imaging, the specimens were prepared by ultra-sonicating the powder samples in ethanol for 15 min prior to measurements to ensure uniform distribution. HRTEM micrographs, Fig. 4 (a, b, c), display the treated and NB samples as aggregates of irregular particles. The aggregation is denser for the treated sample whereas the NB particles have a relatively larger size. Furthermore, Fig. 4 (d, e) demonstrates the scanning electron microscope of the two samples. Both samples show a porous brain-like morphology of accumulated non-uniform particles with different sizes, and the insets display the histograms of the samples. The average particle diameters are 110 ± 32 and 124 ± 33 nm for the treated and the NB samples, respectively. The difference between the XRD crystallite size and FESEM particle size may be explained as a result of small crystals accumulation to attain a lower free energy state. Whenever the adjacent surfaces share the same crystallographic orientation, the adjacent interfaces are eliminated and

the nanoparticles are combined together into a larger particle [50]. Moreover, the inter-particles interaction has also its vital role in the above mentioned discrepancy.

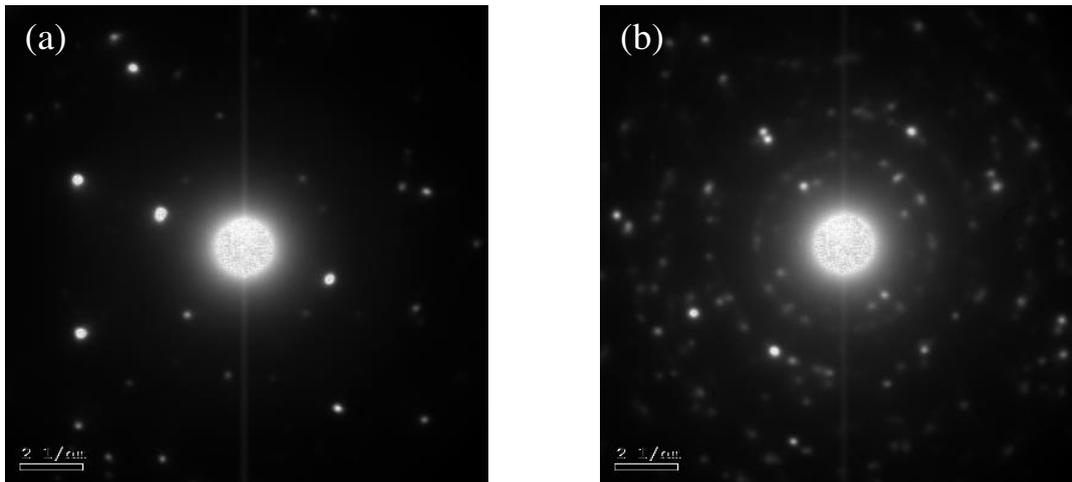


Fig. 5 SAED patterns of a) Treated and b) NB-TiO₂ samples.

The corresponding selected area electron diffraction (SAED) patterns of treated and NB-TiO₂ powders are shown in Fig. 5 (a, b), respectively. The SAED patterns of the NB sample show more diffraction spots and rings of second phases whose brightness is much fainter, so they are badly crystallized and/or partly amorphous [51]. The crystallinity may also be checked by Moiré patterns and their corresponding line analysis. Fig. 4c illustrates the Moiré patterns for the NB-TiO₂ sample. Fig. 6 (a, c) demonstrates the corresponding HRTEM micrograph and line analysis for the treated sample. In contrast to the black sample, the treated sample shows a regular line analysis which indicates no surface distortion. Whereas, Fig. 6b clearly indicates surface distortion for the NB sample. This is even emphasized by its irregular line analysis, Fig. 6d.

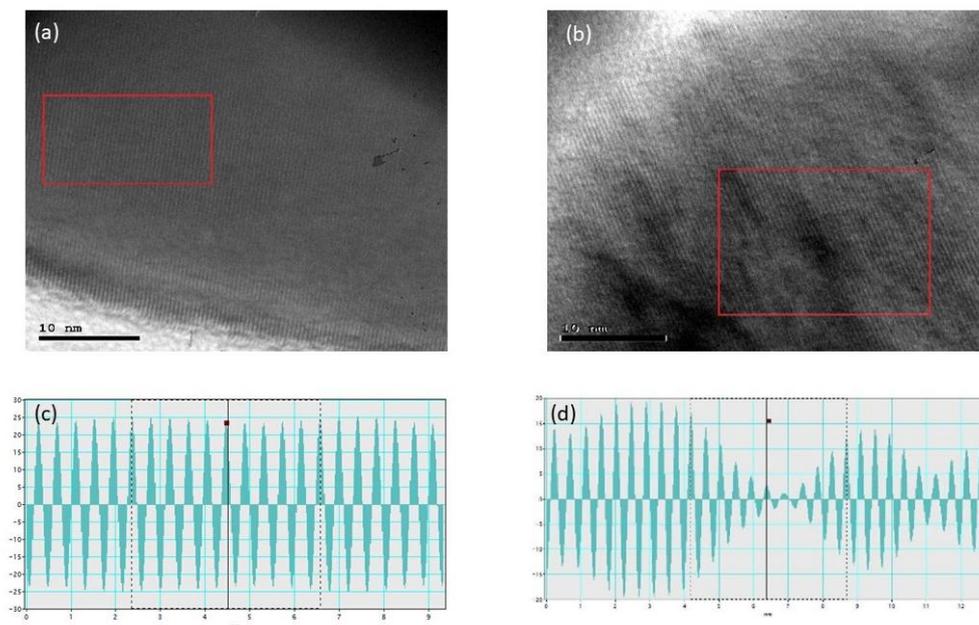


Fig. 6 HRTEM micrographs and Line analysis of a), c) Treated and b), d) NB-TiO₂.

The SEM micrographs in Fig. 7 (a, b) illustrates the adhesion of GO flakes on the PVDF nanofibers surface. Clearly, the micrographs display that GO flakes are intermingled with the nanofibers. The nanofibers seem denser for the pure PVDF polymer. The two micrographs consist of non-uniform fibers, but the degree of non-uniformity is greater for the PVDF-GO hybrid. The average diameters are calculated from the fiber histograms in Fig. 7 (a, b) as 480 and 358 nm for the pure polymeric and hybrid nanofibers, respectively. Generally, the nanofiber diameter and morphology depend on many polymeric solution parameters like viscosity, surface tension, temperature, electrical conductivity, and concentration. Moreover, they are also influenced by device parameters like high voltage value, tip-collector distance, and the collector rotational speed. Specifically, increasing net charge density and the surface tension coefficient favors the formation of smaller diameter fibers [52]. Where, net charge density = jet current x collecting time x concentration x solution density/mass of dry polymer. On the other hand, the polymer jet becomes highly unstable at higher voltage, and thicker fibers are formed but with a high standard deviation of the fiber diameter, which is a consistent description of our data [53]. Moreover, the hybrid fibers show several scattered beads. Typically, the solution viscosity, surface tension, and the net charge density of the electrospinning jet are the main factors of electrospun beads formation [52]. Fig. 7 (c,d) shown FESEM of PVDF-GO/NB-TiO₂ composite nanofibers after crosslinking PVDF-GO composite nanofiber with NB-TiO₂. The morphology of the surface show that NB-TiO₂ stack on the surface of PVDF-GO composite nanofiber.

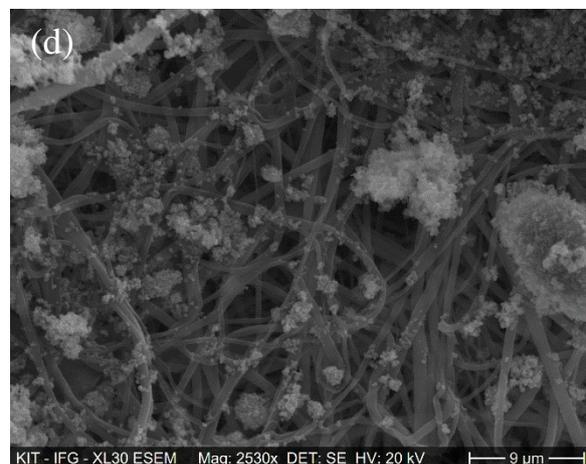
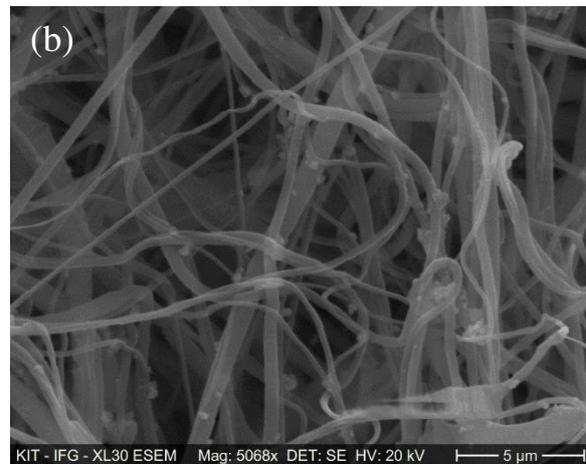
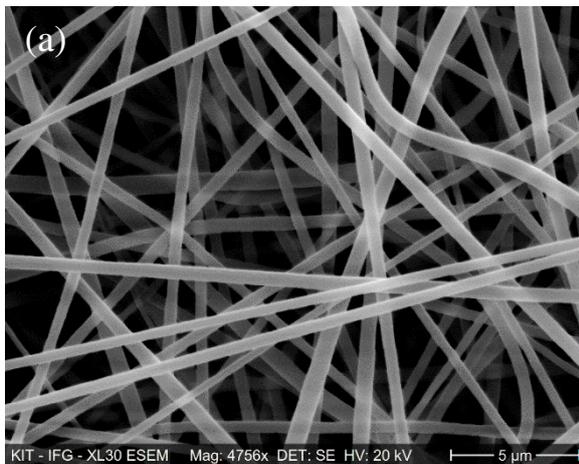


Fig. 7 FESEM of a) PVDF nanofiber, b) PVDF nanofiber with 0.3% GO, c) and d) PVDF-GO/NB-TiO₂ composite nanofibers.

The contact angle is designated as the interface angle between the liquid and contact surfaces. Generally, the degree of wettability of a solid by a liquid is directly measured by the average contact angle. Whenever the contact angle tends to zero, this is referred to as complete wetting; whereas, it is either wettable (hydrophilic) or non-wettable (hydrophobic) depending on whether the angle is smaller or greater than 90⁰, respectively [54]. Fig. 8 demonstrates water droplets on top of nanofibers for the pure PVDF, PVDF-GO, and PVDF-GO/NB-TiO₂ composite nanofibers. The average contact angle measurements indicate that the hybrid PVDF nanofiber with 0.3% GO and 20 mg NB-TiO₂ displays the highest contact angle (138.6⁰). Whereas the lowest contact angle (129.2⁰) occurs for PVDF nanofiber with 0.3% GO. The pure PVDF nanofiber shows a contact angle of 131.7⁰. It is well known that TiO₂ is itself a hydrophobic material, therefore, it's loading to the membrane will increase the contact angle, as expected. However, the effect of adding such a tiny amount of titania is causing merely 7.3% increase of the contact angle.

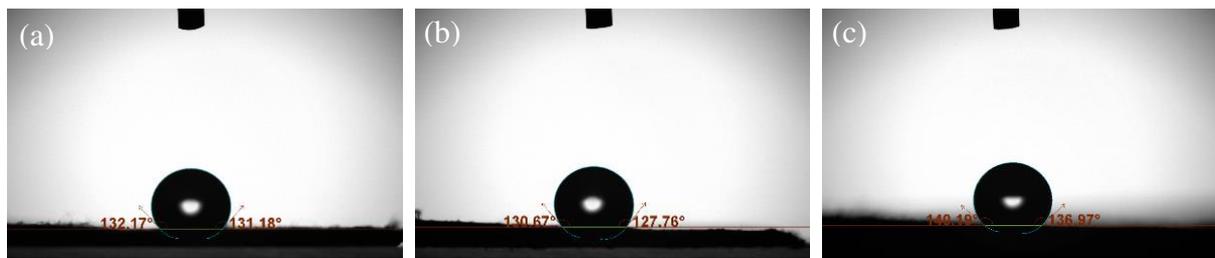


Fig. 8. Contact angle measurements for a) pure PVDF Nanofiber, b) PVDF-GO nanofiber and c) PVDF-GO/NB-TiO₂ composite nanofiber.

Davis and Mott [55] extended Tauc et al. [56] proposition of applying the optical absorbance data to find the band gap energy. They argued that the absorption coefficient α is related to the band gap energy E_g as: $(\alpha h\nu)^{\frac{1}{n}} = A (h\nu - E_g)$ where h is Planck's constant, ν is the photon frequency, A is a constant and n refers to the nature of the electronic transition. Where the allowed direct, indirect transitions are denoted by $n = 1/2, 2$; and $n = 3/2, 3$ for the forbidden direct, indirect transitions, respectively. The absorption processes are normally dominated by the allowed transitions [57]. The absorption coefficient, α , is calculated from the absorbance, Abs , using the relation, $\alpha = \ln 10^{Abs}$ per unit length of the absorbing material [58]. The absorbance measurement of treated and black TiO₂ are shown in Fig. 10a. The absorbance of the NB sample is greatly enhanced relative to that of the treated sample in the UV and visible regions. The spectra of the NB- and T-samples display two main UV peaks at 195 and 275 nm. There is no noticeable relative shift in the two peaks for the two samples. Kubelka-Munk theory was applied to calculate the energy gap from UV-Vis diffuse reflectance spectra. A uniform diffuse irradiation is assumed to propagate through a one-dimensional isotropic slab, assuming no reflection at the boundaries [44, 45]. The Kubelka-Munk function (KMF), $F(R_\infty)$, may be written as [53]: $F(R_\infty) \equiv \frac{(1-R_\infty)^2}{2R_\infty}$, where R_∞ is the reflectance of an infinitely thick layer for

which an additional increase in thickness does not alter its reflectance. This is attained for fine powders at only a few millimeters depth. The KMF is easily formulated as: $F(R_{\infty}) = \frac{K}{S}$, where K and S are the absorption and scattering coefficients, respectively. Moreover, the KMF and the energy band are correlated as: $h\nu F(R_{\infty}) \propto (h\nu - E_g)^n$. The four values of n coincides with the allowed and forbidden transitions mentioned above. Finally, to find E_g , assuming allowed direct transition, a graph of $[ah\nu]^2$ or $[h\nu F(R_{\infty})]^2$ is plotted versus $h\nu$, following Tauc method or Kebulka-Munk theory, respectively. These two graphs are represented in Fig. 9 (b, c). The intersection of the extrapolated linear portion of the graph with $h\nu$ -axis gives the optical energy band. Fig. 9d shows a summary of the attained optical energy gap values.

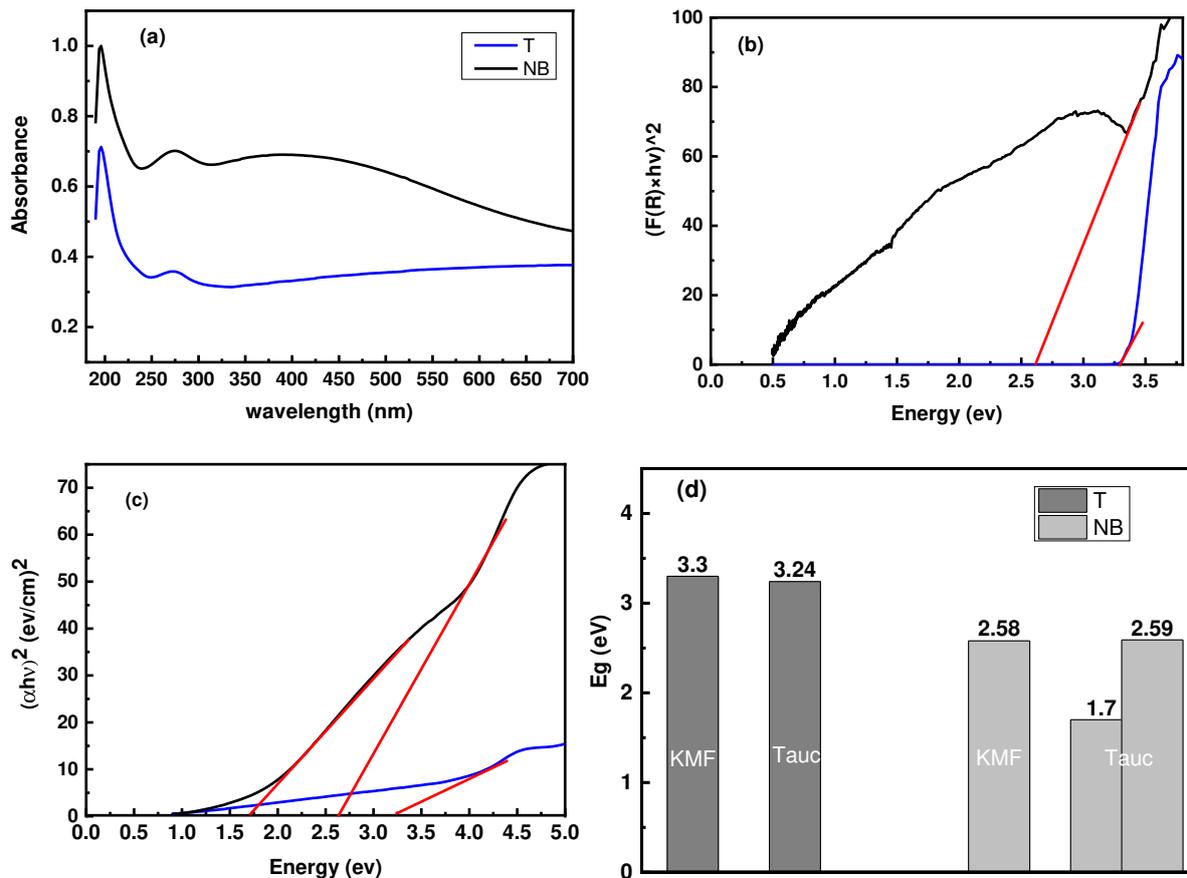


Fig. 9 Optical investigation of T- and NB-TiO₂ a) Absorbance variation with wavelength; energy gap, assuming allowed direct transition, from b) KMF and c) Tauc plots; d) summary of acquired energy gap values.

3.2 Photocatalytic degradation of MG and MB over NB-TiO₂ composite nanofibers

In order to explore the effective photodegradation under visible light irradiation, different catalyst quantities range from 5-20 mg were carried out (Fig. 10a). The maximum degradation of 74 and 39% was obtained at 20 mg of catalyst and 30 min contact time for MG and MB, respectively. The result shows that the higher amount of catalyst provides higher photodegradation efficiency due to the increase of the surface area and the number of active sites available [59]. Different dye pH values of 4, 6, 8, and 10 for 30 min, 5 mg/L of (MB and

MG) and 20 mg NB-TiO₂ was investigated to reveal the optimum degradation efficiency as shown in Fig. 10b. The result shows that pH 8 is the maximum for MG and pH 10 is the maximum for MB. Furthermore, the effect of dyes concentration on degradation efficiency was performed by increasing the concentration to 10 mg/L (Fig. 10d and e). The results reveal that no significant change in degradation efficiency namely decreasing 10 %. MB shows a better dark degradation, however, the photocatalytic degradation is much better for MG. The dye concentration decays monotonically and almost vanished in 120 minutes. These results are attributed to the limitation of hydroxyl radicals and the occupation of the active sites [60, 61].

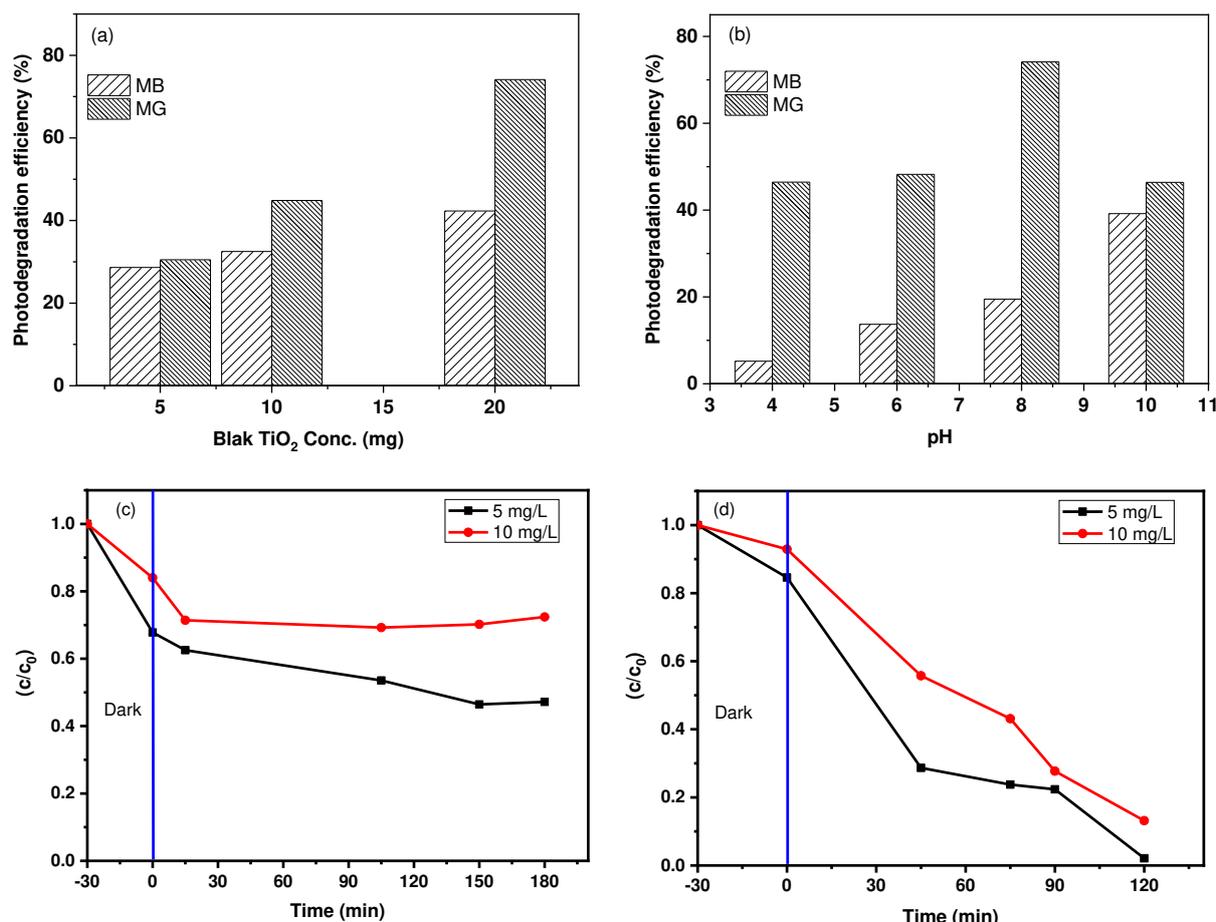


Fig. 10. a) Effect of catalyst amount (5 mg/L, 30 min, and pH 7), b) Effect of pH (5 mg/L, 30 min, and 20 mg), photodegradation of c) MB (pH 10), and d) MG (pH 8).

Incident photons on NB-TiO₂ with quantized energy ($h\nu$) equals to or exceeds the excitation energy (E_g), will produce electron-hole pairs. As a result of this photo-induced process, (e^-/h^+) pairs may be transferred to the NB-TiO₂ surface and become involved in two pathways. These redox reactions could be summarized as shown in Fig. 11b. The main outcome of the two paths is the powerful oxidizing agent, OH^* , as presented in Fig. 12a, which will subsequently interact chemically with the pollutants and transform them into harmless compounds. Hydroxyl groups on NB-TiO₂ profoundly affect its electronic properties and surface chemistry. These surface groups exceptionally affect the charge separation and diffusion of photogenerated electrons and holes which remarkably enhances the photodegradation process. Hydroxyl radicals are

produced in the first path as the hole reacts with water and hydroxide ions and in the second path as the electron reacts with oxygen to produce intervening superoxide radical anions and hydrogen peroxide which ultimately produce hydroxyl radicals as well. Finally, the pollutants adsorbed on the surface of NB-TiO₂ will be dissolved rapidly by the hydroxyl radicals into intermediates which in turn decompose to safe byproducts like CO₂ and H₂O.

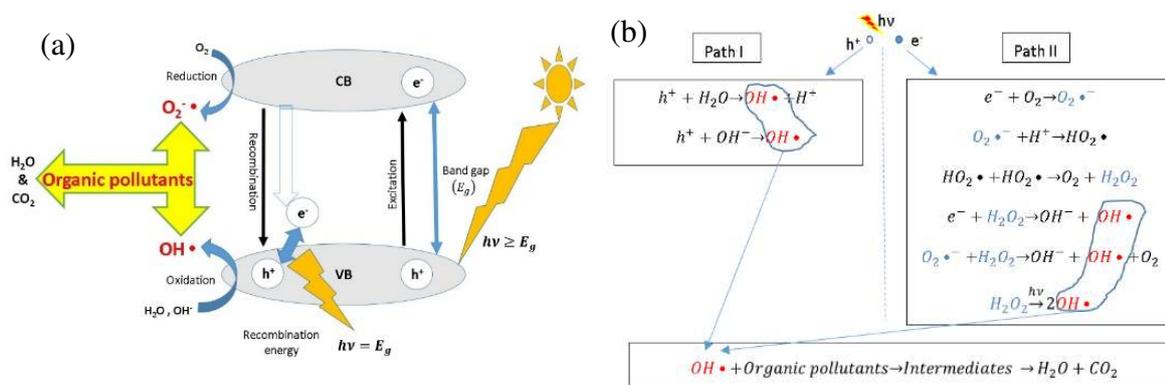


Fig. 11. a) A schematic of photocatalytic degradation of organic pollutants on NB-TiO₂ in the presence of solar light, and b) A summary of the redox reactions at the surface of NB-TiO₂.

4. Conclusions

The nano-black TiO₂, GO and the prescribed membranes were successfully synthesized with no secondary phases recorded. Meanwhile, the HRTEM micrographs and corresponding line analysis clearly displays the black titania surface distortion, repeatedly indicated in the literature. Likewise, the SAED patterns of NB sample reflects its bad crystallinity and even being partly amorphous as may be anticipated from the relatively more diffraction spots and rings of second phases whose brightness is much fainter. Moreover, a percentage drop of at least 20% is reported for the optical energy gap as a result of transforming titanium dioxide into black TiO₂. The degradation of MG and MB depends upon all the reaction parameters such as catalyst amount, pH, and dyes concentration. Furthermore, using the composite nanofiber membrane under visible light for 30 min, the photocatalytic degradation efficiency of MG and MB were found to be 74 and 39%, respectively. The excellent visible photocatalytic activity for MB and MG degradation has been due to its unique narrow energy gap between the oxygen vacancy state and the conduction band, ensuring its excellent visible light absorption to produce photoelectrons and holes in NB-TiO₂.

Abbreviations

Titanium dioxide (TiO₂)
 Graphene Oxide (GO)
 Poly(vinylidene fluoride) (PVDF)
 Malachite green (MG)
 Methylene blue (MB)

Declarations

Not applicable.

Ethics approval and consent to participate

Not applicable.

Consent for publication

Not applicable.

Availability of data and materials

Not applicable.

Competing interests

The authors declare that they have no competing interests.

Funding

Not applicable.

Acknowledgements

Not applicable.

Authors' contributions

MKA: investigation, writing—original draft, writing—review and editing; AM: conceptualisation, methodology, investigation, writing—original draft, writing—review and editing; AS: methodology, investigation, analysis and review; SAK: review and editing. All authors read and approved the final manuscript.

5. References

- [1] M.-W. Zhang, K.-Y.A. Lin, C.-F. Huang, S. Tong, Enhanced degradation of toxic azo dye, amaranth, in water using Oxone catalyzed by MIL-101-NH₂ under visible light irradiation, *Separation and Purification Technology*, 227 (2019) 115632.
- [2] A. Khalil, N.M. Aboamera, W.S. Nasser, W.H. Mahmoud, G.G. Mohamed, Photodegradation of organic dyes by PAN/SiO₂-TiO₂-NH₂ nanofiber membrane under visible light, *Separation and Purification Technology*, 224 (2019) 509-514.
- [3] S.A. Karim, A. Mohamed, M.M. Abdel-Mottaleb, T.A. Osman, A. Khattab, Visible light photocatalytic activity of PAN-CNTs/ZnO-NH₂ electrospun nanofibers, *Journal of Alloys and Compounds*, 772 (2019) 650-655.
- [4] S. El-Sherbiny, F. Morsy, M. Samir, O.A. Fouad, Synthesis, characterization and application of TiO₂ nanopowders as special paper coating pigment, *Applied Nanoscience*, 4 (2014) 305-313.
- [5] T.G. Smijs, S. Pavel, Titanium dioxide and zinc oxide nanoparticles in sunscreens: focus on their safety and effectiveness, *Nanotechnol Sci Appl*, 4 (2011) 95-112.

- [6] S. Mapukata, A.S. Hainer, A.E. Lanterna, J.C. Scaiano, T. Nyokong, Decorated titania fibers as photocatalysts for hydrogen generation and organic matter degradation, *Journal of Photochemistry and Photobiology A: Chemistry*, 388 (2020) 112185.
- [7] N.M. Aboamera, A. Mohamed, A. Salama, T.A. Osman, A. Khattab, An effective removal of organic dyes using surface functionalized cellulose acetate/graphene oxide composite nanofibers, *Cellulose*, 25 (2018) 4155-4166.
- [8] M.M. Abdel-Mottaleb, A. Khalil, T.A. Osman, A. Khattab, Removal of hexavalent chromium by electrospun PAN/GO decorated ZnO, *Journal of the Mechanical Behavior of Biomedical Materials*, 98 (2019) 205-212.
- [9] L. Zhong, X. Li, R. Liu, X. Wei, J. Li, A visible-light-driven photoelectrochemical molecularly imprinted sensor based on titanium dioxide nanotube arrays loaded with silver iodide nanoparticles for the sensitive detection of benzoyl peroxide, *Analyst*, 144 (2019) 3405-3413.
- [10] C.D. Mendonça, V. Rahemi, J. Hereijgers, T. Breugelmans, S.A.S. Machado, K. De Wael, Integration of a photoelectrochemical cell in a flow system for quantification of 4-aminophenol with titanium dioxide, *Electrochemistry Communications*, 117 (2020) 106767.
- [11] A. Khalil, W.S. Nasser, T.A. Osman, M.S. Toprak, M. Muhammed, A. Uheida, Surface modified of polyacrylonitrile nanofibers by TiO₂/MWCNT for photodegradation of organic dyes and pharmaceutical drugs under visible light irradiation, *Environmental Research*, 179 (2019) 108788.
- [12] M.G. Yazdi, M. Ivanic, A. Mohamed, A. Uheida, Surface modified composite nanofibers for the removal of indigo carmine dye from polluted water, *RSC Advances*, 8 (2018) 24588-24598.
- [13] Y.R. Park, K.J. Kim, Structural and optical properties of rutile and anatase TiO₂ thin films: Effects of Co doping, *Thin Solid Films*, 484 (2005) 34-38.
- [14] G.F. Chalastara K, Elouatik S, Demopoulos GP, Tunable Composition Aqueous-Synthesized Mixed-Phase TiO₂ Nanocrystals for Photo-Assisted Water Decontamination: Comparison of Anatase, Brookite and Rutile Photocatalysts, *Catalysts*, 10 (2020) 407.
- [15] M. Batzill, E.H. Morales, U. Diebold, Influence of Nitrogen Doping on the Defect Formation and Surface Properties of TiO_2 Rutile and Anatase, *Physical Review Letters*, 96 (2006) 026103.
- [16] J. Bai, B. Zhou, Titanium Dioxide Nanomaterials for Sensor Applications, *Chemical Reviews*, 114 (2014) 10131-10176.
- [17] X. Chen, L. Liu, P.Y. Yu, S.S. Mao, Increasing Solar Absorption for Photocatalysis with Black Hydrogenated Titanium Dioxide Nanocrystals, *Science*, 331 (2011) 746.
- [18] M.M. Abdel-Mottaleb, A. Khalil, S. Karim, T.A. Osman, A. Khattab, High performance of PAN/GO-ZnO composite nanofibers for photocatalytic degradation under visible irradiation, *Journal of the Mechanical Behavior of Biomedical Materials*, 96 (2019) 118-124.
- [19] N.M. Aboamera, A. Mohamed, A. Salama, T.A. Osman, A. Khattab, Characterization and mechanical properties of electrospun cellulose acetate/graphene oxide composite nanofibers, *Mechanics of Advanced Materials and Structures*, 26 (2019) 765-769.
- [20] J.M. E. Sudova, Z. Svobodova, T. Vesely, Negative effects of malachite green and possibilities of its replacement in the treatment of fish eggs and fish: a review, *Veterinarni Medicina*, 52 (2007) 527-539.
- [21] S.A. Karim, A. Mohamed, M.M. Abdel-Mottaleb, T.A. Osman, A. Khattab, Mechanical Properties and the Characterization of Polyacrylonitrile/Carbon Nanotube Composite Nanofiber, *Arabian Journal for Science and Engineering*, 43 (2018) 4697-4702.
- [22] A. Mohamed, Chapter Eight - Synthesis, Characterization, and Applications Carbon Nanofibers, in: S. Yaragalla, R. Mishra, S. Thomas, N. Kalarikkal, H.J. Maria (Eds.) *Carbon-Based Nanofillers and Their Rubber Nanocomposites*, Elsevier, 2019, pp. 243-257.

- [23] A. Mohamed, W.S. Nasser, B.M. Kamel, T. Hashem, Photodegradation of phenol using composite nanofibers under visible light irradiation, *European Polymer Journal*, 113 (2019) 192-196.
- [24] A. Salimi, A.A. Yousefi, Analysis Method: FTIR studies of β -phase crystal formation in stretched PVDF films, *Polymer Testing*, 22 (2003) 699-704.
- [25] K. Castkova, J. Kasty, D. Sobola, J. Petrus, E. Stastna, D. Riha, P. Tofel, Structure-Properties Relationship of Electrospun PVDF Fibers, *Nanomaterials (Basel)*, 10 (2020) 1221.
- [26] L.Y. Ruan, X.; Chang, Y.; Zhou, L.; Qin, G.; Zhang, X, Properties and Applications of the β Phase Poly(vinylidene fluoride), *Polymers (Basel)*, 10 (2018) 228.
- [27] H. Arami, M. Mazloumi, R. Khalifehzadeh, S. Sadrnezhaad, Sonochemical preparation of TiO₂ nanoparticles, *Materials Letters*, 61 (2007) 4559-4561.
- [28] S. Phokha, S. Pinitsoontorn, S. Maensiri, S. Rujirawat, Structure, optical and magnetic properties of LaFeO₃ nanoparticles prepared by polymerized complex method, *Journal of Sol-Gel Science and Technology*, 71 (2014) 333-341.
- [29] M.A. Ahmed, N.G. Imam, M.K. Abdelmaksoud, Y.A. Saeid, Magnetic transitions and butterfly-shaped hysteresis of Sm-Fe-Al-based perovskite-type orthoferrite, *Journal of Rare Earths*, 33 (2015) 965-971.
- [30] K. Thamaphat, P. Limsuwan, Phase Characterization of TiO₂ Powder by XRD and TEM, in, 2008.
- [31] Z. Xu, T. Wu, J. Shi, K. Teng, W. Wang, M. Ma, J. Li, X. Qian, C. Li, J. Fan, Photocatalytic antifouling PVDF ultrafiltration membranes based on synergy of graphene oxide and TiO₂ for water treatment, *Journal of Membrane Science*, 520 (2016) 281-293.
- [32] X. Cai, T. Lei, D. Sun, L. Lin, A critical analysis of the α , β and γ phases in poly(vinylidene fluoride) using FTIR, *RSC Advances*, 7 (2017) 15382-15389.
- [33] A. Mohamed, W.S. Nasser, T.A. Osman, M.S. Toprak, M. Muhammed, A. Uheida, Removal of chromium (VI) from aqueous solutions using surface modified composite nanofibers, *J Colloid Interface Sci*, 505 (2017) 682-691.
- [34] C. Pasquini, Near Infrared Spectroscopy: fundamentals, practical aspects and analytical applications, *Journal of the Brazilian Chemical Society*, 14 (2003) 198-219.
- [35] A. Mohamed, W.S. Nasser, T.A. Osman, M.S. Toprak, M. Muhammed, A. Uheida, Removal of chromium (VI) from aqueous solutions using surface modified composite nanofibers, *Journal of Colloid and Interface Science*, 505 (2017) 682-691.
- [36] S.G. Ullattil, S.B. Narendranath, S.C. Pillai, P. Periyat, Black TiO₂ Nanomaterials: A Review of Recent Advances, *Chemical Engineering Journal*, 343 (2018) 708-736.
- [37] M. Lohrasbi, In Situ FTIR Study of the Photocatalytic Properties of TiO₂ and Conductivity of Polyaniline, in, University of Akron, 2014.
- [38] J. Trimboli, M. Mottern, H. Verweij, P.K. Dutta, Interaction of Water with Titania: Implications for High-Temperature Gas Sensing, *The Journal of Physical Chemistry B*, 110 (2006) 5647-5654.
- [39] A. Mohamed, T.A. Osman, M.S. Toprak, M. Muhammed, A. Uheida, Surface functionalized composite nanofibers for efficient removal of arsenic from aqueous solutions, *Chemosphere*, 180 (2017) 108-116.
- [40] R.A.S.H.H. Mantsch, Infrared Spectroscopy in Clinical and Diagnostic Analysis, in: *Encyclopedia of Analytical Chemistry*, 2006.
- [41] J. Kong, S. Yu, Fourier Transform Infrared Spectroscopic Analysis of Protein Secondary Structures, *Acta Biochimica et Biophysica Sinica*, 39 (2007) 549-559.
- [42] A. Mohamed, T.A. Osman, M.S. Toprak, M. Muhammed, E. Yilmaz, A. Uheida, Visible light photocatalytic reduction of Cr(VI) by surface modified CNT/titanium dioxide composites nanofibers, *Journal of Molecular Catalysis A: Chemical*, 424 (2016) 45-53.

- [43] C. Drouet, P. Alphonse, A. Rousset, IR spectroscopic study of NO and CO adsorptions on nonstoichiometric nickel–copper manganites, *Physical Chemistry Chemical Physics*, 3 (2001) 3826-3830.
- [44] C. Xu, X. Shi, A. Ji, L. Shi, C. Zhou, Y. Cui, Fabrication and Characteristics of Reduced Graphene Oxide Produced with Different Green Reductants, *PLOS ONE*, 10 (2015) e0144842.
- [45] B. Chen, J.A. Beach, D. Maurya, R.B. Moore, S. Priya, Fabrication of black hierarchical TiO₂ nanostructures with enhanced photocatalytic activity, *RSC Advances*, 4 (2014) 29443-29449.
- [46] C.-C. Wang, P.-H. Chou, Effects of various hydrogenated treatments on formation and photocatalytic activity of black TiO₂ nanowire arrays, *Nanotechnology*, 27 (2016) 325401.
- [47] G. Panomsuwan, A. Watthanaphanit, T. Ishizaki, N. Saito, Water-plasma-assisted synthesis of black titania spheres with efficient visible-light photocatalytic activity, *Physical Chemistry Chemical Physics*, 17 (2015) 13794-13799.
- [48] R. Sanz, L. Romano, M. Zimbone, M.A. Buccheri, V. Scuderi, G. Impellizzeri, M. Scuderi, G. Nicotra, J. Jensen, V. Privitera, UV-black rutile TiO₂: An antireflective photocatalytic nanostructure, *Journal of Applied Physics*, 117 (2015) 074903.
- [49] A. Mohamed, R. El-Sayed, T.A. Osman, M.S. Toprak, M. Muhammed, A. Uheida, Composite nanofibers for highly efficient photocatalytic degradation of organic dyes from contaminated water, *Environmental Research*, 145 (2016) 18-25.
- [50] P.M. Kibasomba, S. Dhlamini, M. Maaza, C.-P. Liu, M.M. Rashad, D.A. Rayan, B.W. Mwakikunga, Strain and grain size of TiO₂ nanoparticles from TEM, Raman spectroscopy and XRD: The revisiting of the Williamson-Hall plot method, *Results in Physics*, 9 (2018) 628-635.
- [51] G. Cheng, F. Xu, F.J. Stadler, R. Chen, A facile and general synthesis strategy to doped TiO₂ nanoaggregates with a mesoporous structure and comparable property, *RSC Advances*, 5 (2015) 64293-64298.
- [52] I.C. H. Fong, D.H. Reneker, Beaded nanofibers formed during electrospinning, *Polymer*, 40 (1999) 4585–4592.
- [53] A.S. Motamedi, H. Mirzadeh, F. Hajiesmaeilbaigi, S. Bagheri-Khoulenjani, M. Shokrgozar, Effect of electrospinning parameters on morphological properties of PVDF nanofibrous scaffolds, *Progress in Biomaterials*, 6 (2017) 113-123.
- [54] S.S. Ray, S.-S. Chen, H.-M. Chang, C.N. Dan Thanh, H. Quang Le, N.C. Nguyen, Enhanced desalination using a three-layer OTMS based superhydrophobic membrane for a membrane distillation process, *RSC Advances*, 8 (2018) 9640-9650.
- [55] N.F.M.a.E.A. Davis, *Electronic Processes in Non-Crystalline Materials*, Oxford Classic Texts in the Physical Sciences, 2012.
- [56] J. Tauc, Optical Properties and Electronic Structure of Amorphous Semiconductors, in: S. Nudelman, S.S. Mitra (Eds.) *Optical Properties of Solids: Papers from the NATO Advanced Study Institute on Optical Properties of Solids Held August 7–20, 1966, at Freiburg, Germany*, Springer US, Boston, MA, 1969, pp. 123-136.
- [57] B.D. Vieszicke, S. Patel, B.E. Davis, D.P. Birnie Iii, Evaluation of the Tauc method for optical absorption edge determination: ZnO thin films as a model system, *physica status solidi (b)*, 252 (2015) 1700-1710.
- [58] T. Tański, W. Matysiak, B. Hajduk, Manufacturing and investigation of physical properties of polyacrylonitrile nanofibre composites with SiO₂, TiO₂ and Bi₂O₃ nanoparticles, *Beilstein Journal of Nanotechnology*, 7 (2016) 1141-1155.
- [59] A. Mohamed, M.M. Ghobara, M.K. Abdelmaksoud, G.G. Mohamed, A novel and highly efficient photocatalytic degradation of malachite green dye via surface modified polyacrylonitrile nanofibers/biogenic silica composite nanofibers, *Separation and Purification Technology*, 210 (2019) 935-942.

- [60] A.M. Khalil, A.I. Schäfer, Cross-linked β -cyclodextrin nanofiber composite membrane for steroid hormone micropollutant removal from water, *Journal of Membrane Science*, (2020) 118228.
- [61] A. Mohamed, S. Yousef, M. Ali Abdelnaby, T.A. Osman, B. Hamawandi, M.S. Toprak, M. Muhammed, A. Uheida, Photocatalytic degradation of organic dyes and enhanced mechanical properties of PAN/CNTs composite nanofibers, *Separation and Purification Technology*, 182 (2017) 219-223.

Figures

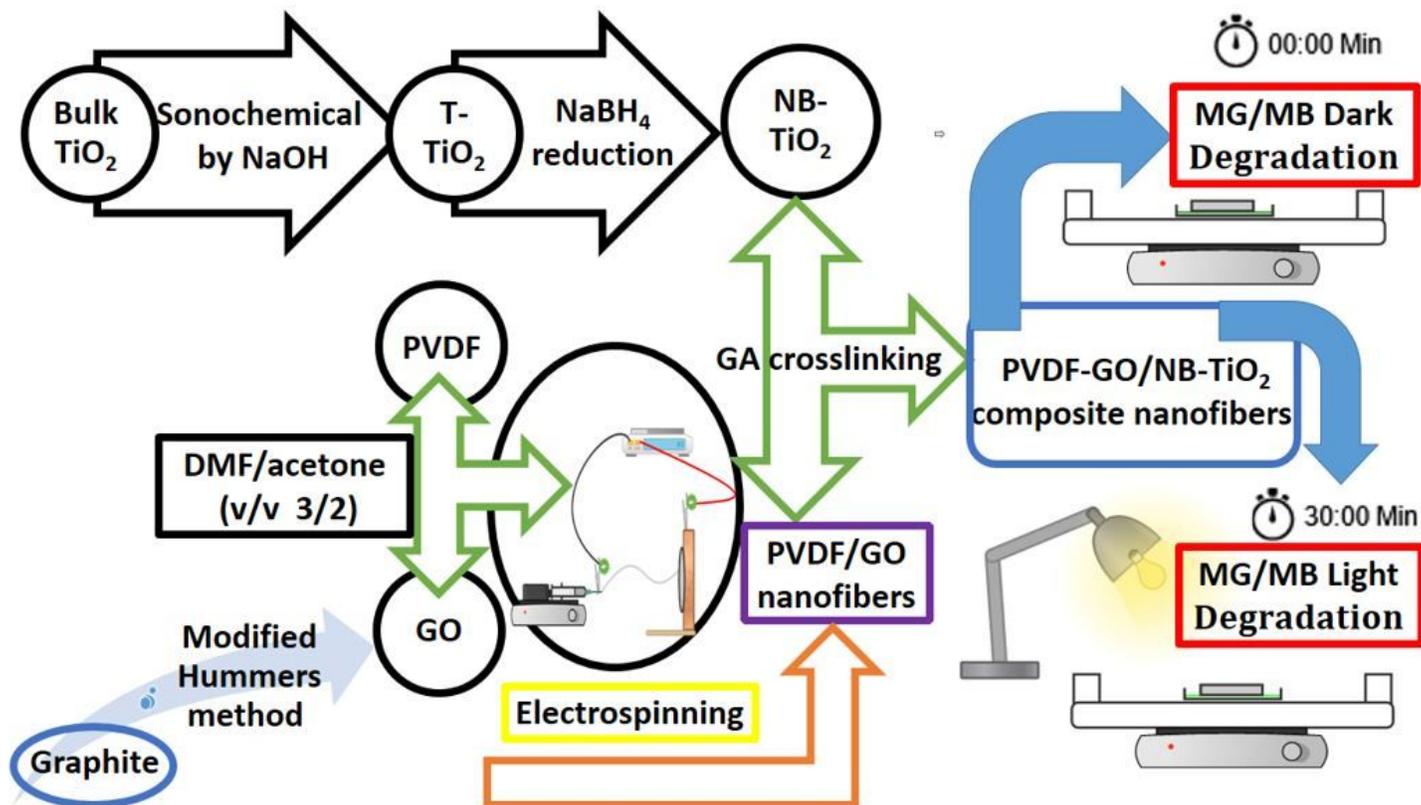


Figure 1

A schematic of the preparation techniques and the experimental procedure followed in this study.

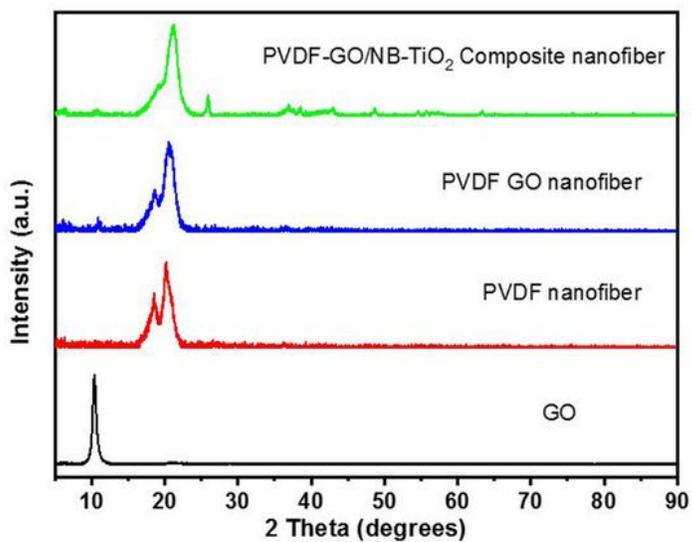
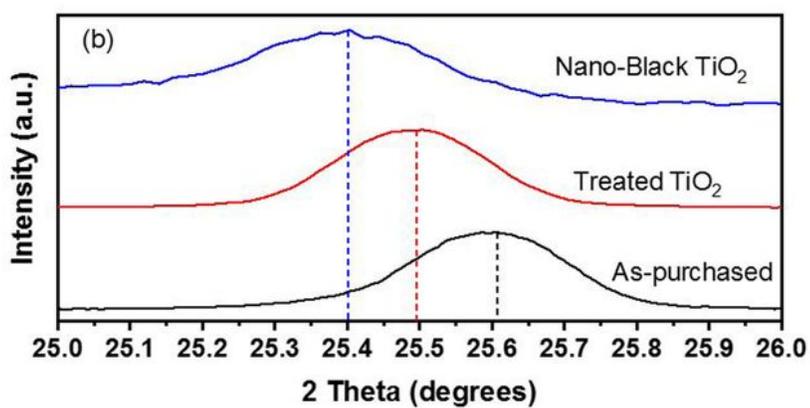
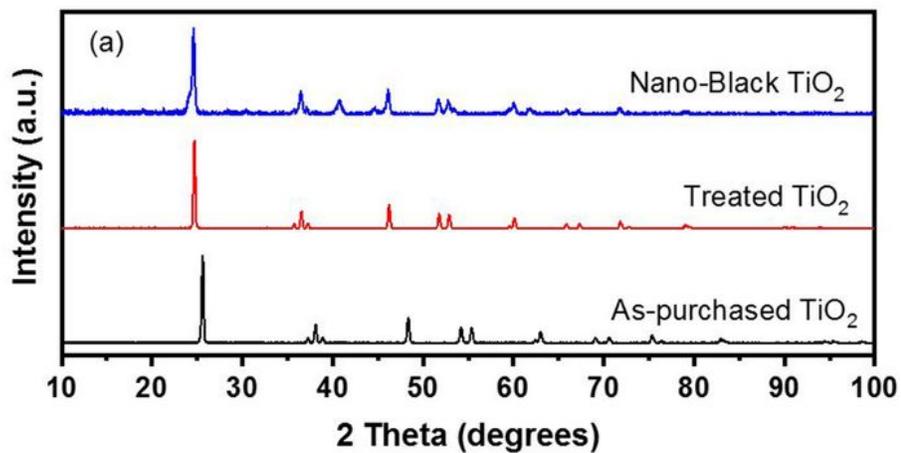


Figure 2

a) X-ray diffraction of as-purchased, treated (T) and nano-black (NB) TiO_2 , b) Deviation of the peak position around 25.60 and c) XRD of GO, PVDF nanofiber, PVDF-GO nanofiber, and PVDF-GO/NB- TiO_2 .

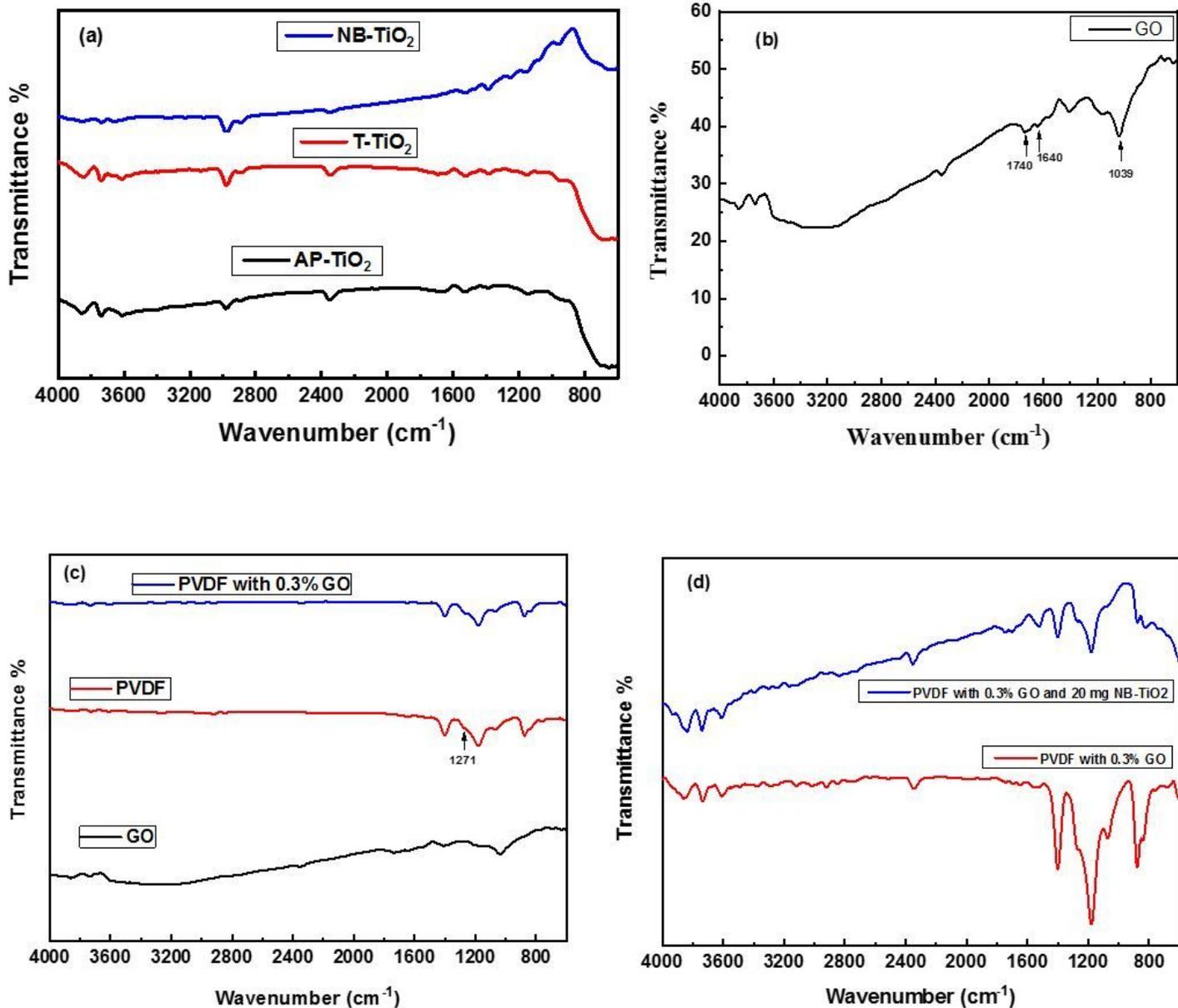


Figure 3

FTIR of a) AP, T and NB-TiO₂, b) prepared GO, c) GO, PVDF nanofiber and PVDF nanofiber with 0.3% GO and d) PVDF nanofiber with 0.3% GO and PVDF nanofiber with 0.3% GO doped with 20 mg NB-TiO₂.

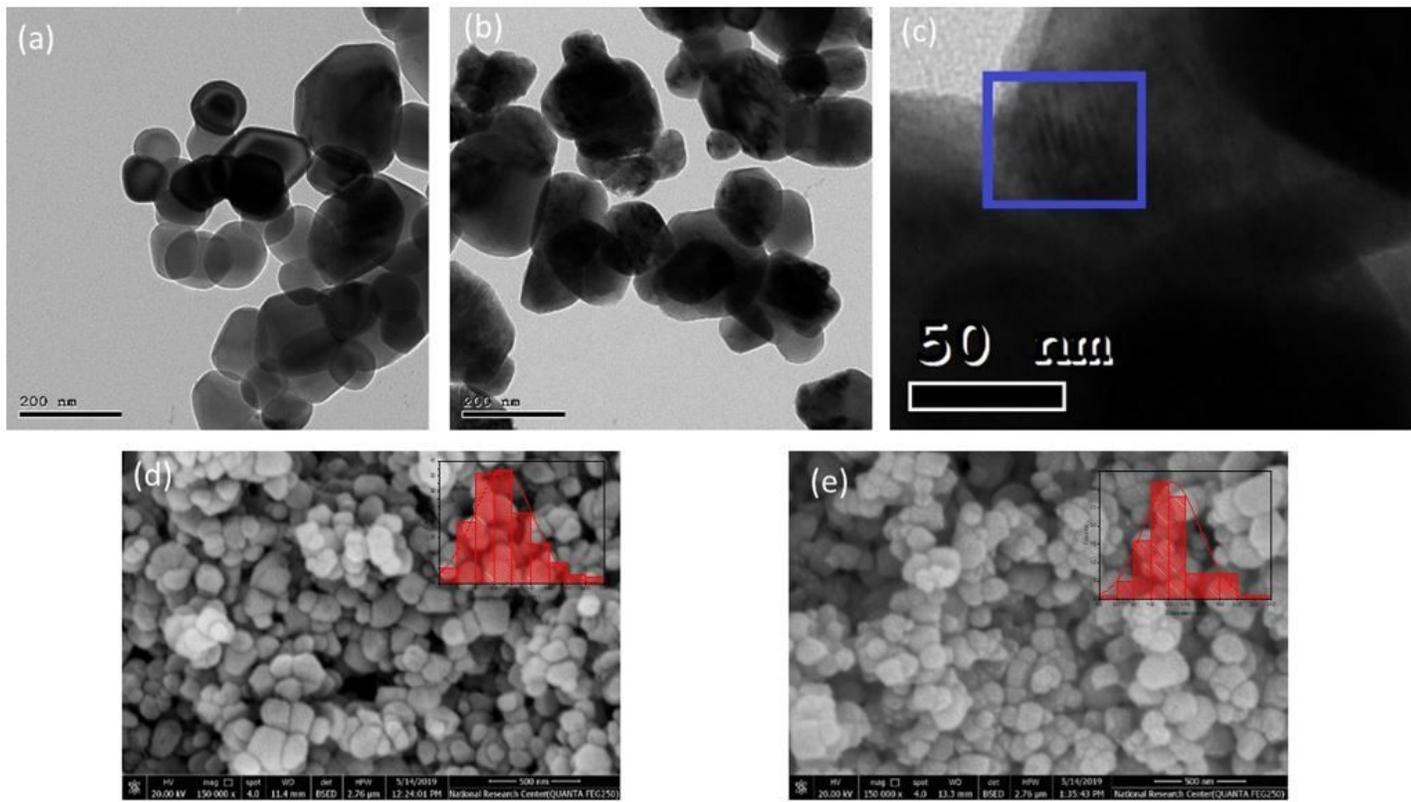


Figure 4

HRTEM of a) T-TiO₂, b) NB-TiO₂ and c) Moiré fringes in NB sample, FESEM of d) Treated and e) NB-TiO₂ nanoparticles, with the corresponding particles distribution as insets.

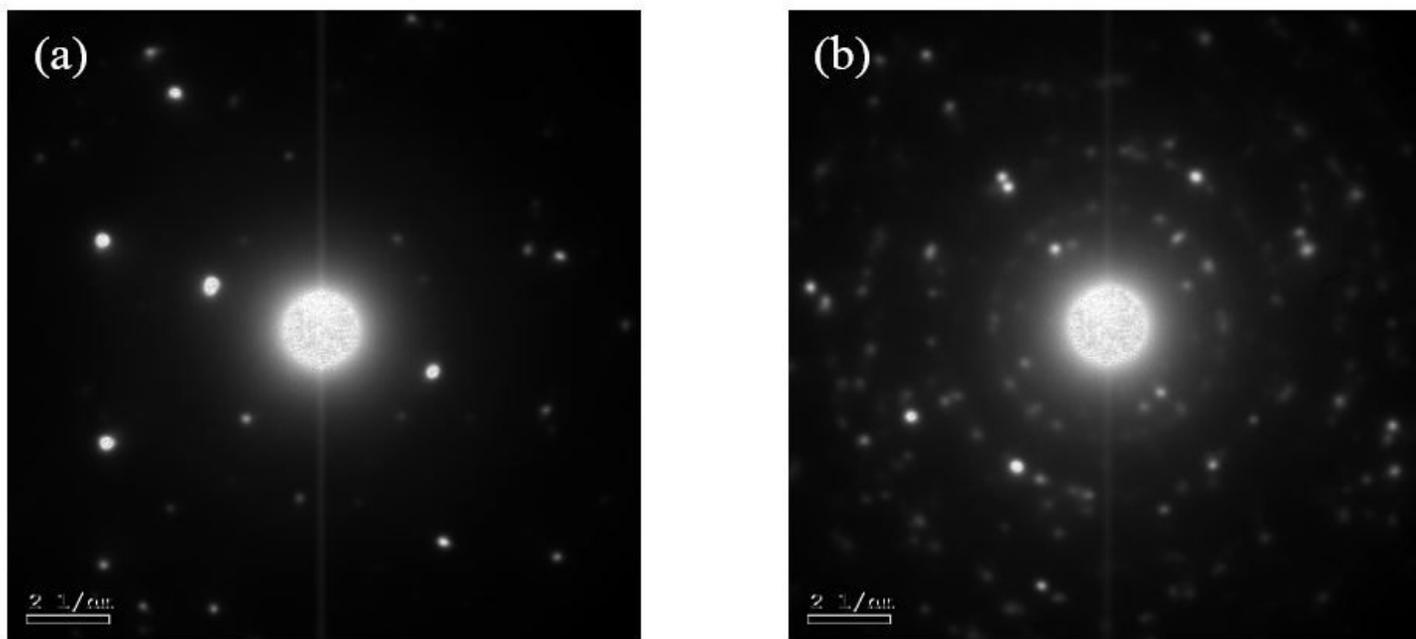


Figure 5

SAED patterns of a) Treated and b) NB-TiO₂ samples.

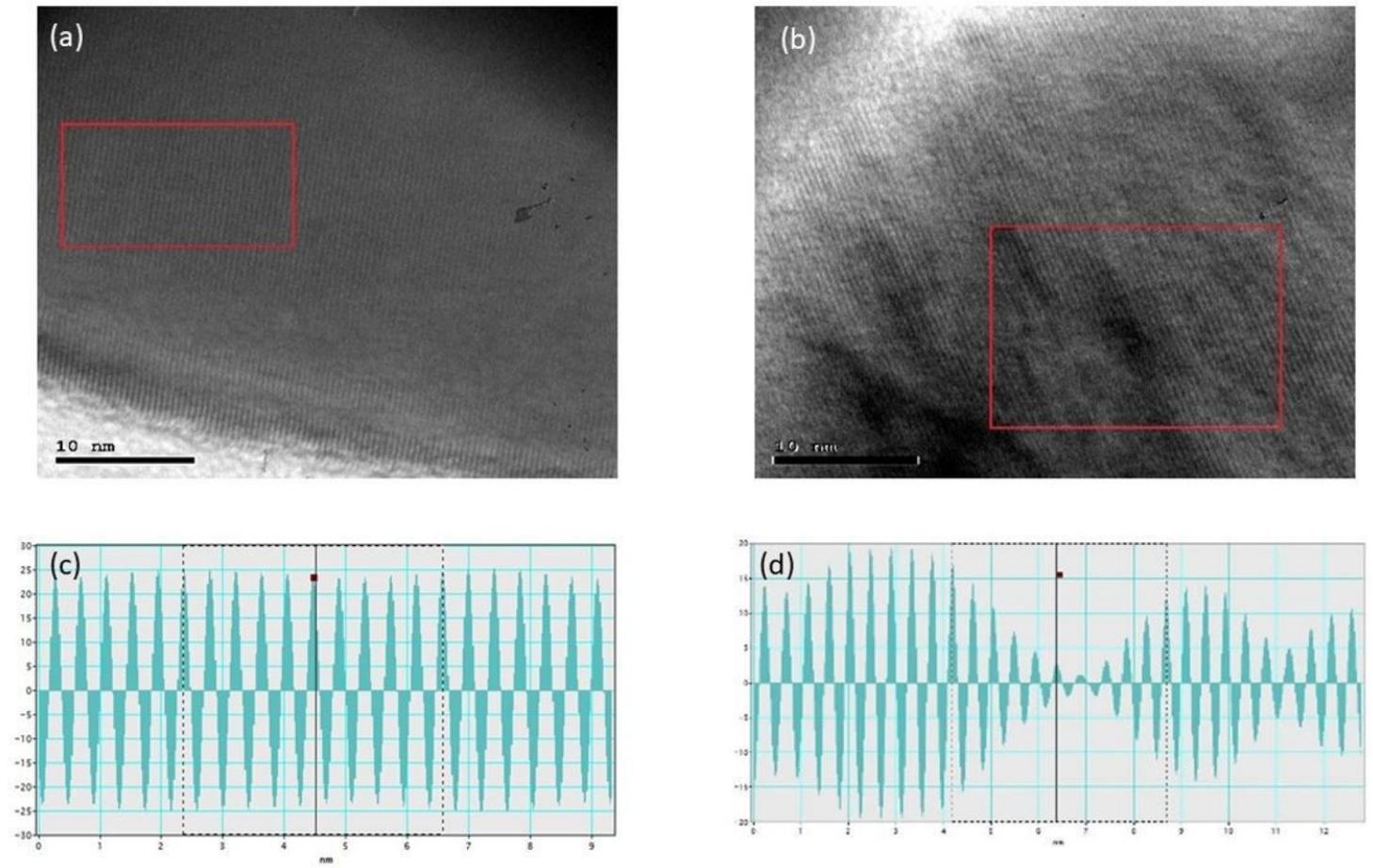


Figure 6

HRTEM micrographs and Line analysis of a), c) Treated and b), d) NB-TiO₂.

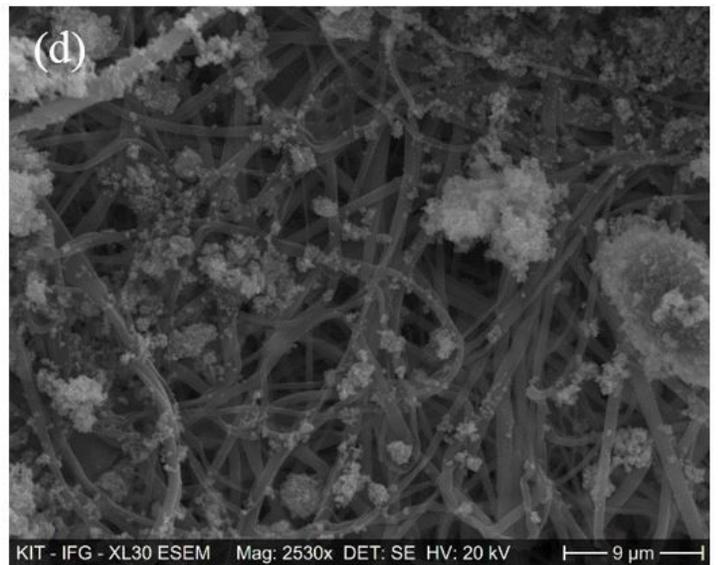
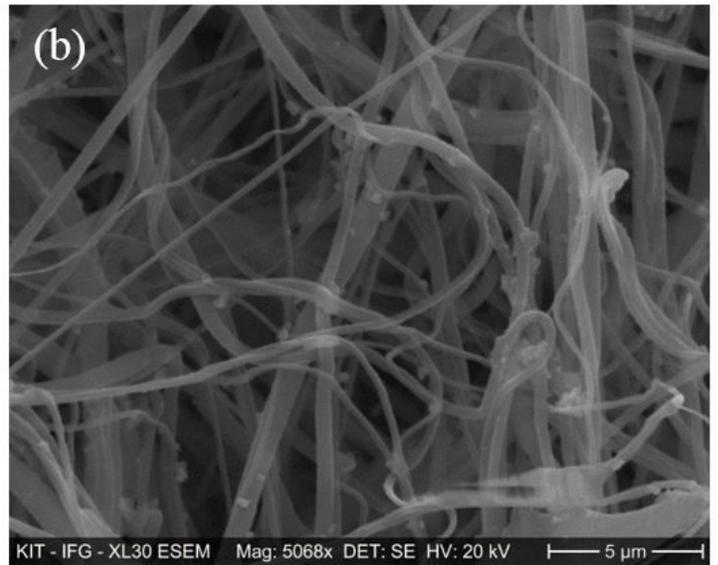
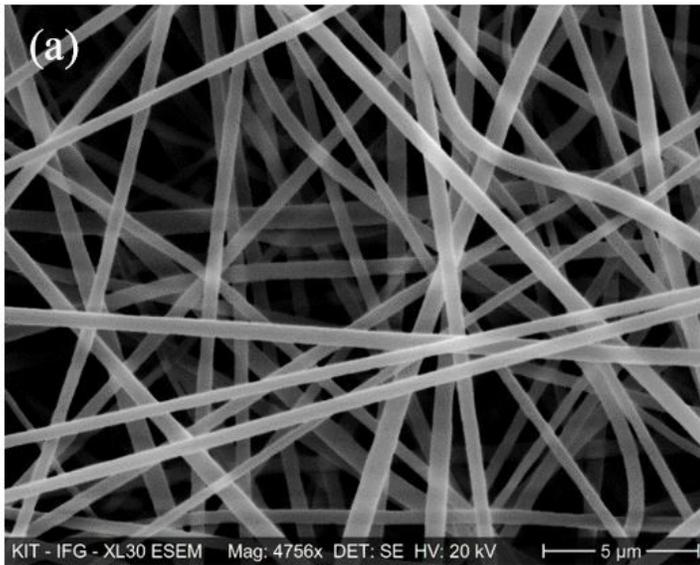


Figure 7

FESEM of a) PVDF nanofiber, b) PVDF nanofiber with 0.3% GO, c) and d) PVDF-GO/NB-TiO₂ composite nanofibers.

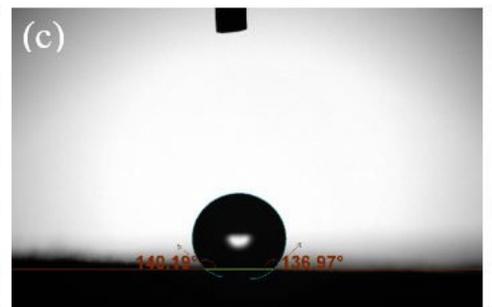
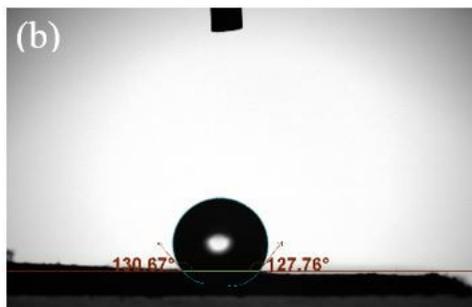


Figure 8

Contact angle measurements for a) pure PVDF Nanofiber, b) PVDF-GO nanofiber and c) PVDF-GO/NB-TiO₂ composite nanofiber.

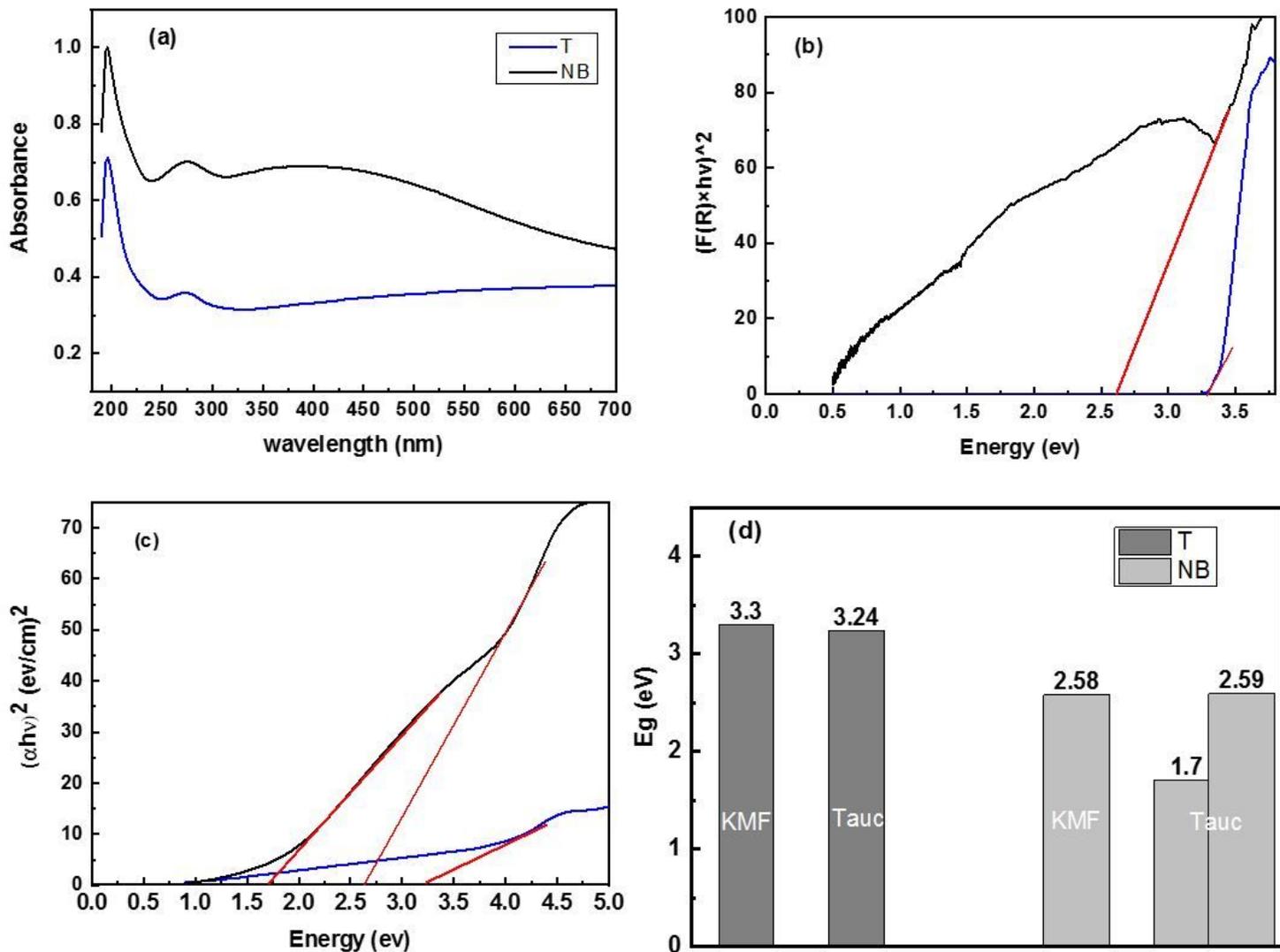


Figure 9

Optical investigation of T- and NB-TiO₂ a) Absorbance variation with wavelength; energy gap, assuming allowed direct transition, from b) KMF and c) Tauc plots; d) summary of acquired energy gap values.

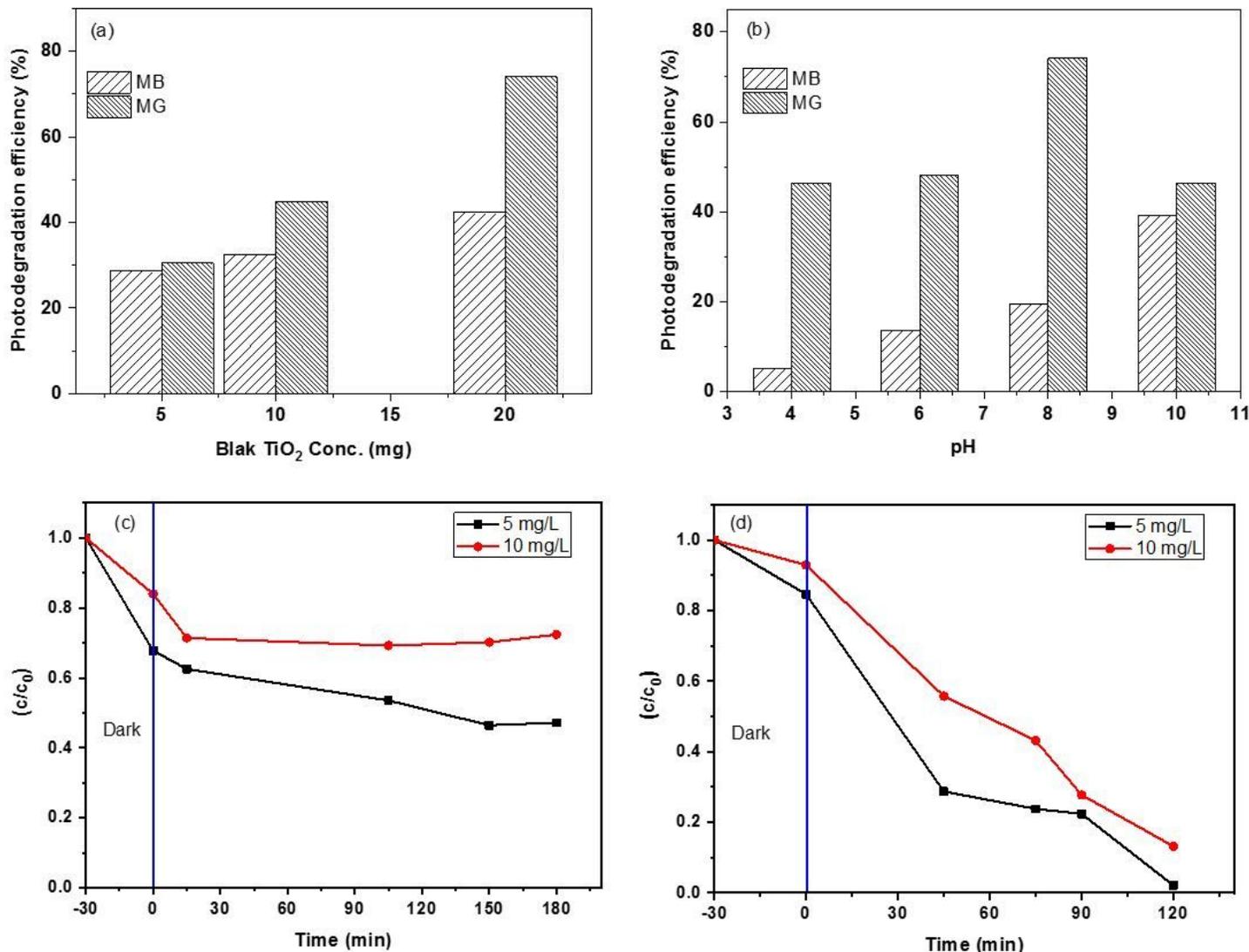


Figure 10

a) Effect of catalyst amount (5 mg/L, 30 min, and pH 7), b) Effect of pH (5 mg/L, 30 min, and 20 mg), photodegradation of c) MB (pH 10), and d) MG (pH 8).

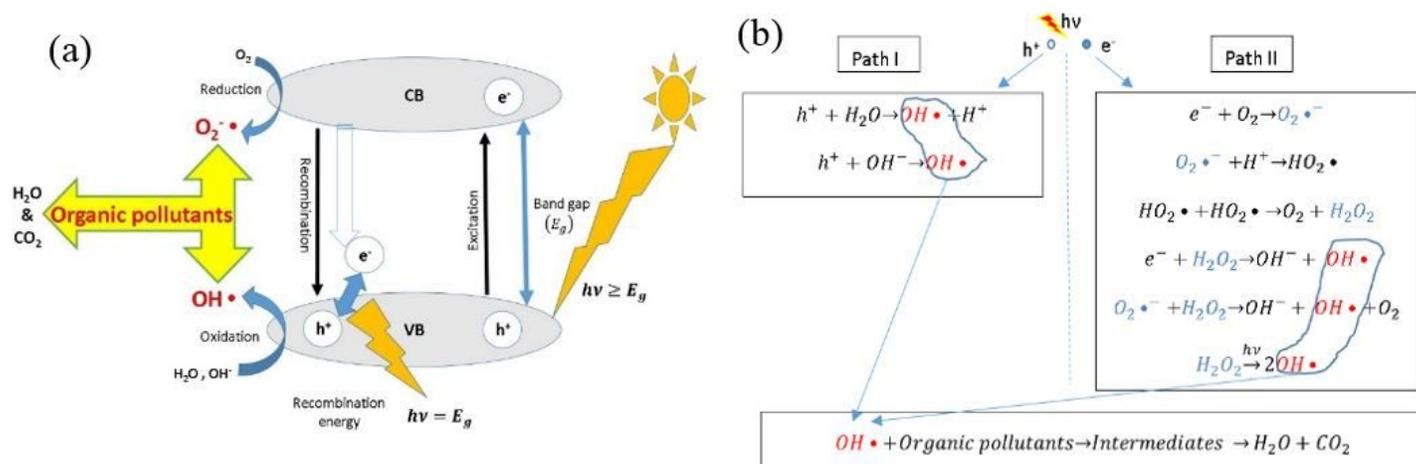


Figure 11

a) A schematic of photocatalytic degradation of organic pollutants on NB-TiO₂ in the presence of solar light, and b) A summary of the redox reactions at the surface of NB-TiO₂.